Quasistatic mechanical behavior of HMX- and TATB-based plastic-bonded explosives

Gaëtane Plassart, Didier Picart, Michel Gratton, Arnaud Frachon, Michael Caliez

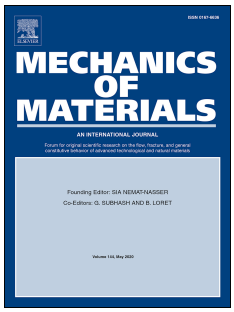

Quasistatic mechanical behavior of HMX- and TATB-based plastic-bonded explosives

Gaëtane Plassart, Didier Picart, Michel Gratton, Arnaud Frachon, Michaël Caliez

PII: S0167-6636(20)30603-7

DOI: https://doi.org/10.1016/j.mechmat.2020.103561

Reference: MECMAT 103561

To appear in: *Mechanics of Materials*

Received Date: 3 January 2020

Revised Date: 6 August 2020

Accepted Date: 6 August 2020

Please cite this article as: Plassart, Gaë., Picart, D., Gratton, M., Frachon, A., Caliez, Michaë., Quasistatic mechanical behavior of HMX- and TATB-based plastic-bonded explosives, *Mechanics of Materials* (2020), doi: https://doi.org/10.1016/j.mechmat.2020.103561.

QUASISTATIC MECHANICAL BEHAVIOR OF HMX- AND TATB-BASED PLASTIC-BONDED EXPLOSIVES

Gaëtane Plassart[1], Didier Picart[1*], Michel Gratton[2], Arnaud Frachon[2], Michaël Caliez[2]

[1] CEA DAM Le Ripault, F-37260 Monts, France
[2] INSA CVL, Univ. Orléans, Univ. Tours, LaMé, EA 7494, F-41000, Blois, France
[*] Corresponding author: didier.picart@cea.fr

Abstract

Data on the macroscopic quasistatic mechanical behavior of pressed HMX- and TATB-based plastic-bonded explosives (PBXs) are listed in this paper. This review shows that (1) few characterizations are available for TATB-based PBXs. This gap is filled in this paper. An extensive database is detailed for the CEA M2 explosive composition. The HMX and TATB database then enables selection of the deformation mechanisms to be considered: viscoelasticity, damage-induced anisotropy and its effectivity (i.e.: whether or not the damage is influenced by the loading direction), plasticity with kinematic and isotropic hardenings, pressure and temperature dependencies and asymmetric failure threshold. The review also shows that (2) HMX- and TATB-based materials share close elastic and ultimate properties when the compositions (binders, solid volume fractions) and the mechanical behavior of the two crystals differ. The constitutive laws proposed in the literature are reiterated. In our opinion, a universal law could be proposed in the near future, each material being considered by its own set of parameters. The objective of this paper is to draw up the guidelines for model improvement.

Keywords

Plastic-bonded explosives. Constitutive law. Experimental characterization. Induced anisotropy.

1. Introduction

When designing a pyrotechnic structure, simulations must be performed to assess mechanical strength. This step consists, in particular, in developing and implementing a constitutive law for the energetic material. In addition, the thermomechanical stresses that such a material undergoes during its life cycle can alter its microstructure and potentially modify its mechanical and/or reactive behavior. To guarantee the safety and reliability of pyrotechnic structures, understanding and modelling the thermomechanical behavior of these materials is essential.

Among the existing energetic materials, pressed explosives are granular materials with a small amount of polymeric binder. This paper focuses on the thermomechanical characterization of some pressed explosives, from experimental study to modelling, highlighting the state of the art in this field. Our objective is to determine if a unified model could be proposed in the near future for plastic-bonded explosives (PBXs). This study is limited to the quasistatic domain with strain rates of 10^{-6} to 10^{-3} s^{-1} and strains in the order of one percent, which justifies the small strains assumption. The temperature ranges between -30°C and +80°C and the confinement pressure between 0.1 and 10 MPa. The post-peak behavior is outside the field of this study, with safety margins requiring the stress path to remain below the maximum stress.

The plastic-bonded explosives of interest are made of HMX (octahydro-1,3,5,7-tetranitro-1,3,5,5,7-tetrazocine) or TATB crystals (1,3,5-triamino-2,4,6-trinitrobenzene). The CEA (Commissariat à l'Energie Atomique et aux Energies Alternatives - French Alternative Energies and Atomic Energy Commission) has developed several explosive compositions such as M1 and M2, composed respectively of more than 95 wt% HMX or TATB, mixed with polymeric binders and densified by hot isostatic compression. The residual porosity is less than 5%. Other TATB- and HMX-based PBXs

frequently mentioned in the literature are PBX-9502 (95 wt% TATB, 5 wt% Kel-F 800 binder), LX-17-1 (92.5 wt% TATB, 5 wt% Kel-F 800 binder), PBX-9501 (95 wt% HMX, 2.5 wt% Estane binder and BDNPA/F), LX-14 (95.5 wt% HMX, 4.5 wt% Estane binder) and EDC-37 (91 wt% HMX, 1 wt% NC binder and DNEB/TNEB). These explosives are formed by isostatic compression at relatively high temperatures and pressures (Picart, 1993; Thompson and Wright, 2004). They are isotropic in their initial state with a low residual porosity. The literature reports that, until the 1980s, PBX-9502 could be densified by uniaxial compression (Blumenthal et al., 1999; Skidmore et al., 1998), leading to an initial anisotropic macroscopic behavior caused by the perpendicular alignment with the pressing direction of the TATB crystals (Schwarz et al., 2013).

The mechanical properties of PBXs have been studied since the 1980s and quasistatic constitutive laws have been developed. The characterization of the material being the first step, phenomena must be isolated and identified from data. A review of the various tests carried out on these materials is proposed in section 2 of this paper. Published experimental data on PBXs are essentially limited to uniaxial compression or tension tests, at various temperatures, in which only longitudinal strains are measured (Blumenthal et al., 1999; Browning et al., 1984; Buechler, 2012a, 2012b; Buechler et al., 2013; Ellis et al., 2005; Funk et al., 1996; Gagliardi and Cunningham, 2007; Gray et al., 1998; Skidmore et al., 1998; Thompson, 2002; Thompson et al., 2010; Zubelewicz et al., 2013). Some compression tests on an HMX-based PBX under various confinement pressures can be mentioned (Wiegand et al., 2011) as well as a torsion test on PBX-9501 (Gagliardi and Cunningham, 2009). Dynamic Mechanical Analysis (DMA) has been performed on PBX-9501 and PBX-9502 (Thompson et al., 2012). The database on M1 is much more complete (see section 2 and Benelfellah, 2013; Benelfellah et al., 2017; Caliez et al., 2014; Le et al., 2010; Picart et al., 2014; Picart and Brigolle, 2010; Picart and Pompon, 2016).

The constitutive laws of PBXs can be divided into macroscopic and micromechanical models. To the authors' knowledge, the first macroscopic models appeared in the 1980s in France and in the United States. A first model of non-linear viscoelastic behavior, pressure- and temperature-dependent, was established by Belmas et al. (1982). This model is limited to monotonic loadings. Peeters and Hackett (1981) have reproduced the time-dependence of the behavior of pressed explosives. They developed two unidimensional models: a law for compression and creep for monotonic loadings, and a linear viscoelastic model able to simulate unloading and reloading (see also Browning et al., 1984). A famous macroscopic model is the SCRAM (Statistical CRAcks Mechanics) model (Dienes, 1978, 1996; Dienes et al., 2006). SCRAM is based on the strain rates additivity and contains an elastoplastic part with kinematic hardening describing the behavior of the matrix, plus anisotropic damage describing the microcrack network (nucleation, growth and coalescence). IsoSCRAM (Addessio and Johnson, 1990) is a simplified version of SCRAM with isotropic damage and without microcracks coalescence. The reader will also find the ViscoSCRAM model (Bennett et al., 1998; Hackett and Bennett, 2000) based on IsoSCRAM with a viscoelastic part. Recently, Liu et al. (2019) have modified the ViscoSCRAM model adding a Bodner-Partom viscoplasticity and changing the microcracking kinetics. Most of the other models focus on the viscosity of these polymer-bonded materials, and all of them include damage. Le et al. (2010) have developed a Maxwell viscoelastic model coupled with isotropic damage and pressure-dependent plastic behavior with isotropic hardening and non-associated flow. Buechler (2012b, 2013) has added combined isotropic/kinematic hardening to the viscoplasticity. Zubelevicz et al. (2013) have introduced different damage rates in tension and compression coupled with viscoplasticity. Lastly, a microplane model with anisotropic damage added to non-associated plasticity with isotropic hardening was proposed by Benelfellah et al. (Benelfellah, 2013; Benelfellah et al., 2014, 2017; Picart et al., 2014).

The micromechanical models help us understand the influence of the different components on the macroscopic behavior since they capture the mechanisms at the grain scale (Ambos et al., 2015; Arora et al., 2015; Clements and Mas, 2004; Gasnier et al., 2018; Tan et al., 2005, 2007; Wu and Huang, 2009). However, at the engineering level, these models cannot yet be used to simulate the explosive behavior in a pyrotechnic structure due to a huge calculation cost. This paper focuses exclusively on macroscopic models of the quasistatic behavior of pressed explosives.

Firstly, the state of the art of experimental characterization of the quasistatic behavior of PBXs is presented in section 2 of this paper. This review provides an opportunity to consider all the data already available for the widely characterized M1 composition. In section 3, an extensive experimental

campaign performed on the M2 TATB-based PBX is presented, and the data is exploited in section 4. A list of the deformation mechanisms to be considered in a constitutive law can be provided based on these three previous sections. Already published macroscopic thermomechanical models are detailed and compared in section 5. The discussion allows conclusions to be drawn on the relevance of these models for HMX- and TATB-based PBXs. Guidelines are proposed for future model improvements.

2. State of the art in experimental characterization of PBXs

2.1. HMX-based PBXs

Since 2000, the CEA and the Gabriel LaMé Laboratory have undertaken an extensive experimental campaign to characterize the various behavioral features of the material M1. This database includes monotonic and cyclic compressions at 20°C and under atmospheric pressure, for four strain rates from 10^{-6} s^{-1} to 10^{-3} s^{-1} ; monotonic and cyclic compressions at 20°C under 5 and 10 MPa, at 10^{-5} s^{-1}; monotonic and cyclic tension tests at 0°C, 20°C, 35°C and 50°C under atmospheric pressure, at 10^{-5} s^{-1} (Benelfellah, 2013; Caliez et al., 2014; Gratton et al., 2009; Le, 2007; Le et al., 2010; Picart and Brigolle, 2010; Rja Fi Allah, 2006); cyclic compressions at 0°C, 35°C and 50°C under atmospheric pressure, at 10^{-5} s^{-1} (Le, 2007); heterogeneous tests such as the Brazilian test, biaxial tension (plate bending), channel-die test, Iosipescu test and three-point bending, at 20°C under atmospheric pressure, at a strain rate of about 10^{-5} s^{-1} (Benelfellah, 2013; Le, 2007; Picart and Pompon, 2016); alternate tension-compression and compression-tension at 20°C under atmospheric pressure, at 10^{-5} s^{-1} (Benelfellah, 2013; Picart and Brigolle, 2010); as well as a dynamic mechanical analysis (DMA) campaign (Picart and Brigolle, 2010). For each uniaxial or triaxial test of these papers, the longitudinal and transversal strains are given. Furthermore, each cycle of cyclic tests consists of four steps: a loading, a stress relaxation of at least 30 minutes, an unloading to zero stress and a strain recovery of at least 30 minutes. The authors studied the influence of temperature, pressure and loading rate. In particular, the elastic modulus increases with pressure up to 10 MPa and then remains constant (highly confined tests are presented in Vial, 2013). This highlights the influence of the initial porosity, completely closed under a 10 MPa pressure. Thus, the elastic modulus calculated under this confinement appears as the intrinsic Young's modulus of the material. The viscoelasticity of M1 has been characterized and the failure criterion has been obtained by multiaxial tests and conventional tension and compression tests. Cyclic compression tests revealed the inelastic strains and a load-induced anisotropy, resulting in a unilateral effect observed during the alternated tests.

For other HMX-based PBXs, such as the well-known PBX-9501, the literature shows monotonic uniaxial compression tests at room temperature and 60°C for strain rates from 10^{-6} s^{-1} to 10^{-3} s^{-1} (Buechler, 2012a; Ellis et al., 2005; Funk et al., 1996; Gray et al., 1998) as well as tests with load-unload-recovery cycles at -15°C, 23°C and 50°C with rates in the range of 10^{-5} s^{-1} and 10^{-4} s^{-1} during loading and 10^{-3} s^{-1} during unloading (Buechler, 2012b; Buechler et al., 2013). Monotonic tension tests are also mentioned at -18°C and 10^{-4} s^{-1} (Thompson, 2002) and at room temperature at $2x10^{-5}$ s^{-1} (Ellis et al., 2005) as well as load-unload-recovery cyclic tests at 23°C and about 10^{-4} s^{-1} (Buechler et al., 2013). For all these tests, only longitudinal strains are represented as a function of stress. A DMA campaign has been conducted on PBX-9501 (Thompson et al., 2012a). Torsion tests, with and without axial stress, have been performed at 25°C and 0.08 $deg.s^{-1}$ (Gagliargi and Cunningham, 2009). A three-point bending test at a displacement rate of 0.0212 $mm.s^{-1}$, for a specimen measuring 75x15x10mm (Hackett and Bennett, 2000) and another at 0.2 $mm.s^{-1}$ for a specimen measuring 114x102x12mm (Ellis et al., 2005) are also mentioned. Furthermore, several publications are related to Brazilian tests and the failure mode of the material (intergranular or transgranular) (Chen at al., 2007; Liu and Thompson, 2010; Rae et al., 2002; Williamson et al., 2007).

From the DMA measurements (Thompson et al., 2012a), PBX-9501 is very viscous from -30°C. The influence of the loading rate and the asymmetry between tension and compression were also highlighted. Tests at several temperatures were carried out by the various authors, but none of them presents a comparison of the behavior under various temperatures.

The influence of confinement pressure up to 140 MPa on EDC-37 has been studied by Wiegand et al. (2011) (monotonic compressions under confinement). The stress-strain curves show that the more

the containment increases, the higher is the peak stress and the more the post-peak phase disappears. At high confinement (above 7 MPa), a long almost horizontal plateau appears. The authors calculate an elastic modulus at the beginning of the stress-strain curve (no details are given). The evolution of this module according to the confinement follows two regimes: it doubles between 0 and 7 MPa but varies very little beyond that. Tests with load-unload-reload were also carried out under various confinements. The authors say that at low confinement (up to 7 MPa) a decrease of the elastic modulus is observed when reloading. At high confinement, the modulus does not evolve. In addition, from a test conducted at a pressure above 30 MPa, the authors show that the yield strength (estimated for a 2% strain) has almost doubled. However, doubts can be expressed about calculating a plasticity threshold at 2% strain on a quasi-brittle material. According to the authors, over the pressure range of 0 to 7 MPa, a damage mechanism would be predominant, while beyond that a plastic flow would govern the behavior.

Lastly, acoustic emissions measurements have been made by Ellis et al. (2005) during compression, tension and three-point bending tests on EDC-37. In this method, the appearance of a crack generates an elastic wave which can be measured and analyzed. For EDC-37, the measured cracking remains very low or even zero as long as the stress/strain response is linear. The non-linearity that appears in compression is very progressive and cracking is observed. In tension/flexure, the response is practically linear (brittle fracture), so cracking only occurs during fracture.

Post-failure microscopies on a PBX-9501 sample subjected to a Brazilian test (Chen at al., 2007; Rae et al., 2002; Williamson et al., 2007) show that the predominant cracking mode is intergranular, by decohesion of grain interfaces. However, Williamson et al. (2007) note that for tests performed below the glass transition temperature of the binder (about -40°C), the failure is transgranular.

The asymmetric nature of the behavior between tension and compression has been observed, but no alternating loading has been achieved. Measurements of transversal strains are never given, which means that no conclusions can be made about a possible induced anisotropy of these materials.

Recently, Buechler and coworkers (Buechler, 2012b; Buechler et al., 2013) applied the experimental procedure used on M1 to characterize PBX-9501, but only longitudinal strains are recorded. From load-unload-reload cycles, irreversible strains are detected. Assuming isotropic hardening due to lack of data, the longitudinal plastic strains are plotted as a function of the cycle maximum stress, and then these values are subtracted from the overall curves. The loading curves thus reconstructed can be considered elastic. Since they are not superimposed due to softening at each cycle, the authors assume the effect of the damage. Thus, this work on damage is more a matter of modelling than characterization.

2.2. TATB-based PBXs

Some data obtained on our TATB-based material M2 have already been published. The stress-strain curve of a cyclic uniaxial compression test, performed at 10^{-5} s^{-1} at room temperature, is presented in two papers (Ambos et al., 2015; Gasnier et al., 2018). Let us note that the ratchet growth phenomenon (cycles of temperature without mechanical loading yields irreversible strain) has never been observed for this material. For other TATB-based PBXs, the experimental database mainly includes monotonic uniaxial compression tests performed between 10^{-5} s^{-1} and 10^{-3} s^{-1} for temperatures from -52°C to 74°C (Blumenthal et al., 1999; Skidmore et al., 1998; Thompson et al., 2010; Zubelewicz et al., 2013), with creep phase (Gagliardi and Cunningham, 2007) or with load-unload cycles (Browning et al., 1984). There are also data on the tension behavior, in monotonic loading from 10^{-5} s^{-1} to 10^{-3} s^{-1} for temperatures from -52°C to 74°C (Thompson, 2002; Thompson et al., 2010; Zubelewicz et al., 2013) and two papers provide tension failure data for different temperatures and strain rates (Idar et al., 2000; Thompson et al., 2012a). In these papers, only longitudinal strains are given, as a function of stress or time. There are also in the literature some monotonic (Cunningham et al., 2013) and cyclic (Thompson et al., 2012b) thermal expansion tests, as well as a DMA campaign (Thompson et al., 2012a). The compression of a perforated plate in its center has been performed (Liu and Thompson, 2014) with measurement of the strain field by digital image correlation. Finally, it should be mentioned that an internal report from the Los Alamos laboratory written by Shunk in 2013 reviews the tests performed on the PBX-9502. Unfortunately, the majority of the references have not been published in the open literature.

The DMA test performed by Thompson et al**.** (2012) shows that the viscosity of the PBX-9502 increases significantly from +25°C. For this material, temperature tends to make it more ductile while the strain rate 10^{-3} and 10^{-5} s^{-1} has very little influence on its behavior at -52°C (Zubelewicz et al., 2013). Asymmetry of the behavior between tension and compression is also observed.

The experimental data on HMX- and TATB-based PBXs are summarized in Table 1.

Table 1*. Mechanical tests performed on HMX- and TATB-based PBXs in the literature. The last column CEA-M2 is a list of the data provided in this paper.*

		PBX-9501 LX-14 EDC-37 (HMX-based)	PBX-9502 LX-17 (TATB-based)	CEA-M1 (HMX-based)	CEA-M2 (TATB-based)
Uniaxial compression	Long. / transv. strains	√ / no	√ / no	√ / √	√ / √
	Temperature	-15°C to 60°C	-52°C to 74°C	0°C to 50°C	-30°C to 80°C
	Strain rate	10^{-6} s^{-1} to 10^{-3} s^{-1}	10^{-5} s^{-1} to 10^{-3} s^{-1}	10^{-6} s^{-1} to 10^{-4} s^{-1}	10^{-6} s^{-1} to 10^{-4} s^{-1}
	Creep / relaxation		√	√	√
	Load – unload cycles	√	√	√	√
	References	[15,16,18,31,32, 38]	[12,14,32,58,64, 72]	[7,20,37,42,43,55]	
Uniaxial tension	Long. / transv. strains	√ / no	√ / no	√ / √	√ / √
	Temperature	-18°C and 20°C	-52°C to 74°C	20°C	-30°C à 80°C
	Strain rate	10^{-5} s^{-1} to 10^{-4} s^{-1}	10^{-5} s^{-1} to 10^{-3} s^{-1}	10^{-5} s^{-1}	10^{-6} s^{-1} to 10^{-4} s^{-1}
	Creep / relaxation			√	√
	Load – unload cycles	√		√	√
	References	[18,31,62]	[62,64,72]	[7,20,37,42,43,51, 55]	
Torsion	Shear strains	√			√
	Temperature	25°C			20°C
	Strain rate	0.08 deg/s			0.01 deg/s
	Creep / relaxation				
	Load – unload cycles				√
	References	[34]			
Triaxial compression	Long. / transv. strains	√ / no		√ / √	√ / √
	Pressure	0.6 to 140 MPa		5 and 10 MPa	
	Temperature	20°C		20°C	20°C
	Strain rate	$5x10^{-4}$ s^{-1}		10^{-5} s^{-1}	10^{-5} s^{-1}
	Creep / relaxation			√	√
	Load – unload cycles			√	√
	References	[68]		[7,20,37,42,43,55]	
Alternative loadings	Long. / transv. strains			√ / √	√ / √
	Temperature			20°C	20°C
	Strain rate			10^{-5} s^{-1}	10^{-5} s^{-1}
	Creep / relaxation				√
	Load – unload cycles				√
	References			[7,51]	
Other tests	DMA	-30°C to +70°C [65]	-25°C to +116°C [65]	-100°C to +100°C [51]	0°C to +90°C
	Multiaxial tests	Brazilian test [25,44,53,69]	Compression of perforated plate [45]	Brazilian test, channel-die, plate bending [7,42,52]	Brazilian test, channel-die, equibiax. comp. bending test

3. Characterization of the TATB-based material M2

A substantial experimental database is necessary to characterize the complex behavior of the PBXs and to justify the modelling choices. While the HMX-based material M1 was extensively characterized (see section 2), data will now be provided for a TATB-based explosive composition. The tests performed on M2 are described in the current section, the analysis of the various curves being reported in the next section.

3.1. Material

M2 is composed of about 95% by weight of TATB grains bonded by a thermoplastic binder. The M2 fabrication has two successive steps. In the first, the explosive crystals are coated with a thin layer of polymeric binder. The mean diameter of TATB grains is about 50 µm and millimetric meta-grains are obtained by granulation. Next, the granules are vacuum-packed in a tight elastomer bag, before being submitted to several cycles of isostatic compression at a temperature of about 150°C and a 200 MPa pressure cycle (Picart, 1993). The temperature is chosen to soften the binder. After cooling, a coherent material is obtained which enables machining samples to be taken. The compaction process eliminates most of the initial porosity, the residual porosity being of only a few percent. Figure 1 shows a micrograph of the material M2. The color variations are due to the strong anisotropy of the TATB grains. However, the orientation of the grains and the binder being randomly distributed, the material is initially isotropic on a macroscopic scale. All the tests described in this paper have been performed on the same batch.

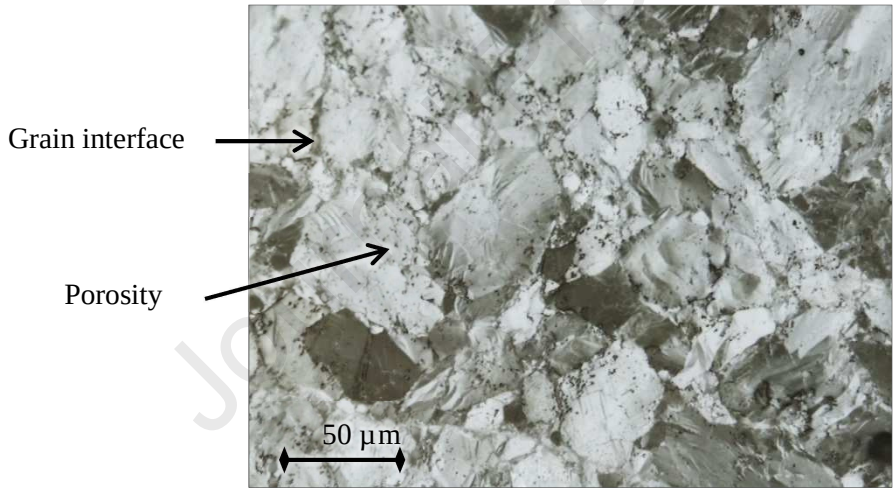

Figure 1*. Micrograph of material M2. The color variations are due to the strong anisotropy of the TATB crystals. Porosity is mainly located inside the grains (small black dots) and at the grain/grain interfaces.*

3.2. Experimental procedure

A list of the tests carried out on M2 in the quasistatic range is given in Table 1 (right column). Unless otherwise stated, the operating procedure of the tests is as follows. The test machine used was a Zwick Z100, a compression/traction machine with a 100 kN load cell. Two other machines were on occasion used: a Metravid DMA instrument, and an Instron compression/torsion machine ElectroPuls^{TM} E10000 whose capacities are ±100 Nm and ±7 kN. The geometry of the specimens was in the centimeter range. Consequently, the applied force rarely exceeded ±10 kN. Since the strains never reached 2%, the variation in cross-section during the test was negligible and the infinitesimal strain theory was available. Thus, the stress was calculated from the force and the initial effective area of the specimen. For compression and tension tests, two strain gauge rosettes were glued opposite each other in the center of the specimen (Vishay M-Bond 200 adhesive). Each rosette had two measuring grids arranged at an angle of 0°/90° (Kyowa KFGS-2-120-D16-11). For torsion tests, three rosettes

were glued at 120° around the central diameter of the specimen. Each rosette had three measuring grids arranged at an angle of -45°/0°/+45° (Kyowa KFGS-2-120-D17-11). The grids of each gauge were two millimeters long, so the strain was measured on a large surface compared to the grain size and small enough compared to the specimen size. The strains correspond to the average of the two opposite gauges. The tests were strain-controlled from one gauge at the reference rate of 10^{-5} s^{-1}, at room pressure and temperature (unless otherwise stated). Each test was repeated three times to ensure a minimum repeatability of the results. Among the three curves, the test representing the mean response was selected and plotted on the graphs discussed in this paper. The results scatter is shown on the curves by the dispersion at the maximum stress. The mean of the maximum stress and the corresponding strains are represented by a point and the tests dispersion is represented by a line.

On the graphs, the stress is represented in absolute value, except for alternate loading tests for which the usual convention is used (negative stress in compression). The nomenclature used is as follows: σ_{11} is the tension/compressive stress calculated from the force cell and the initial dimensions of the specimen; σ_{12} is the shear stress calculated on the external radius of the specimen from the measured torque because that is where the gauges were glued but also where the stress was the greatest; ε_{11}, ε_{22} and ε_{12} are respectively the strains in the longitudinal (negative in compression), transversal (positive in compression) and shear directions; they correspond to the average of the gauge measurements.

3.3. Dynamic mechanical analysis (DMA)

Dynamic mechanical analysis (DMA) tests were carried out in the temperature range from 0°C to 90°C to characterize the material. The samples were 8x8x8mm rods glued on the machine plates. A sinusoidal strain of 0.016% amplitude was imposed, to subject the specimen to tension/compressive cycles with a null average stress at a frequency of 2 to 60 Hz. Measurements had shown that over these frequency and temperature ranges the material behavior is reversible and linear.

The difference in the stress and strain signals amplitude leads to (1) the amplitude $|E^*|$ of the complex elastic modulus and (2) a phase shift (loss factor $\tan\delta$). The real and imaginary elastic moduli, E' and E'', are evaluated as follows: $E' = |E^*|\cos\delta$ and $E'' = |E^*|\sin\delta$. Considering the high stiffness of this material, measurements were corrected by removing the machine stiffness. The uncertainty on the measurement of E' is 4% while that of E'' rises to 40% due to the low viscosity of such material.

These moduli are plotted as a function of the logarithm of the inverse of the frequency f for each temperature. A reference temperature is defined (here 0°C) and, from the time-temperature equivalence principle, the other temperature curves are shifted by a coefficient $a_{t\theta}$ in order to form the master curves. The shift function is a polynomial function determined automatically by minimization of the gap between two consecutive isotherms (T is the temperature in Celsius):

$$\log_{10}\left(\frac{1}{a_{t\theta}}\right) = 8.031\text{x}10^{-4}\,T^2 + 4.930\text{x}10^{-2}\,T + 4.631\text{x}10^{-2} \quad (1)$$

Thus, in Figure 2, the lowest reduced times correspond to the lowest temperature (0°C) and the longest times to the highest temperature (90°C).

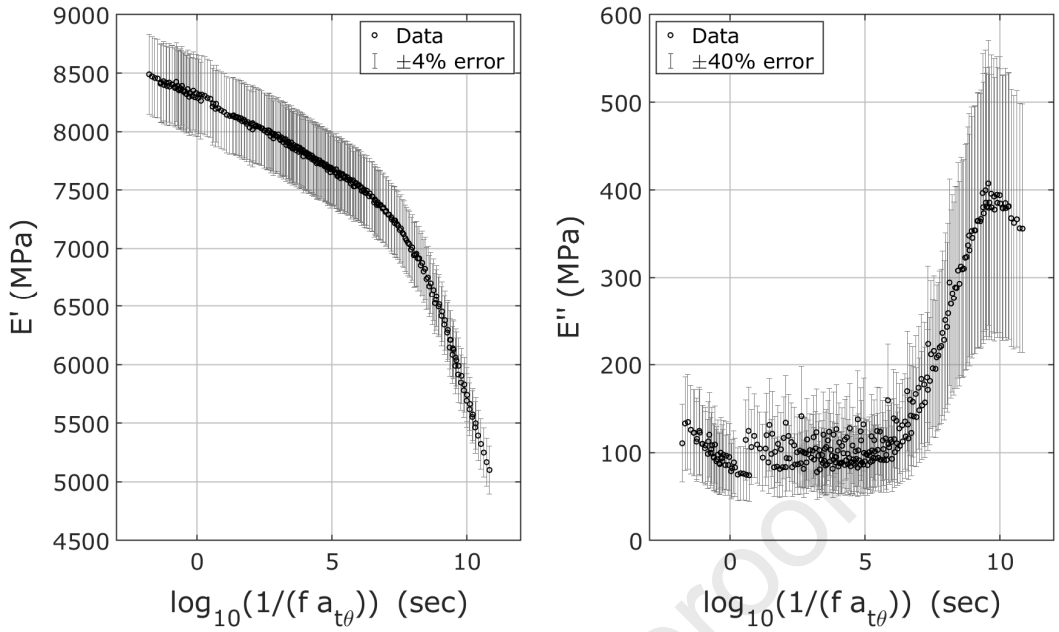

Figure 2*. Real (E') and imaginary (E'') elastic moduli of M2 with respect to the reduced time where f is the frequency of the sinusoidal loading. Master curves (black dots) show a relative strain rate- and temperature-independence while the temperature does not exceed 50-60°C.*

3.4. Uniaxial monotonic loadings

Monotonic uniaxial compression, tension and torsion tests were performed at ambient temperature and pressure. The stress-strain curves are given in Figure 3. The compression samples (cylinders 20 mm high and 10 mm in diameter) were placed between two lubricated compression plates. The tension samples (150 mm high and dog-bone-shaped), with a 10 mm-sided square base, were held by two clamping jaws. For the torsion tests, the samples were hollow dog-bones, 60 mm high, 18 mm in outer diameter and 9 mm in inner diameter. These tests were controlled at $0.01°.s^{-1}$, which corresponds to a shear strain rate of around 10^{-5} s^{-1}. No axial force was applied. The maximum stress dispersion was around 1 MPa. The spread observed at the peak of the compressive test is due to the flat response (plateau) of the material.

3.5. Alternating tension and compression loadings

An experimental campaign of alternative tension/compressive tests was performed on M2. Two tests were conducted: (1) a compression up to 30 MPa (~ 0.95 σ_{max}, where σ_{max} is the maximum compressive stress) followed by a tension loading to failure, and (2) a traction up to 7 MPa (~ 0.95 σ_{max}, where σ_{max} is the maximum tension stress) followed by a compressive loading to failure. Dog-bone-shaped samples with a cylindrical base 10 mm in diameter and 20 mm in height were used.

The experimental data show that the failure stress is the same for alternative tests as it is for monotonic tests. The curve of the compression/tension test is given in Figure 4. There is a defect on the curve linked to the machine software when the force sign changes. Concerning the tension/compression test (not presented here), the tension unloading curve was similar to the loading curve. The global curve of the test overlaps with the tension and compression monotonic curves.

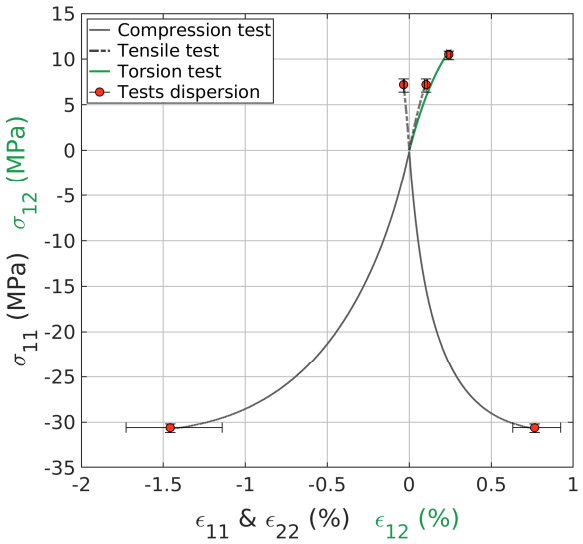

***Figure 3**. Stress-strain curves of compression (black solid lines), tension (black dashed lines) and torsion (green solid lines) tests showing a nonlinear response and an asymmetric behavior.*

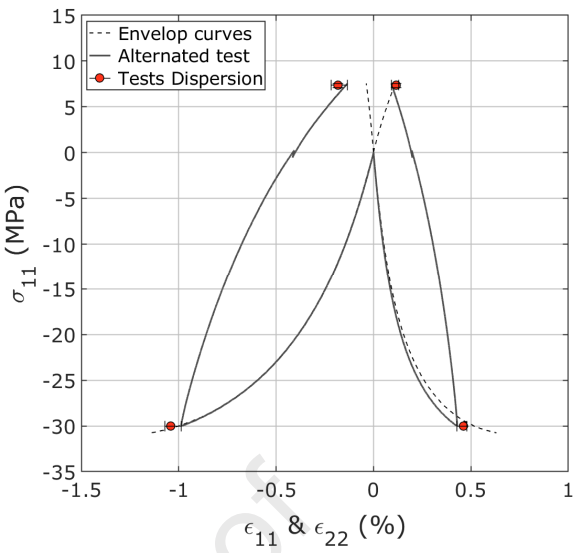

***Figure 4.** Alternating compressive/tension test (solid lines) compared to monotonic compression and tension curves (dashed lines). The compression loading changes the tension response.*

3.6. Pressure-, temperature- and strain rate-dependence

Compression and tension tests at several temperatures and strain rates are presented in Figure 5 and Figure 6. The procedure was identical to the simple compression and simple tension tests at room temperature as already described. To guarantee the temperature setting, specimens were conditioned for at least two hours before the test. In Figure 6, the tension tests at 20°C at 10^{-6} and 10^{-4} s^{-1} are not represented despite having been performed, because the rate effect is negligible at this temperature.

To study the influence of the confinement, monotonic triaxial compressive tests at various confinements (2.5 MPa, 5 MPa and 10 MPa) were carried out. Cylindrical specimens 50 mm in diameter and 100 mm in height were used, on which two strain gauge rosettes were glued at 0°/90°. The sample was placed in a confinement chamber installed inside a sealed elastomer bag. Then, the chamber was filled with water until the desired confinement pressure was reached. Afterwards, a uniaxial stress was applied at the reference strain rate of 10^{-5} s^{-1} until failure. The influence of the pressure is shown in Figure 7.

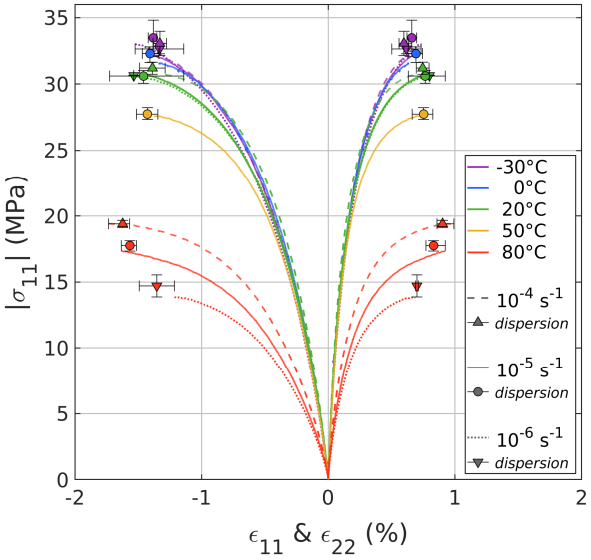

Figure 5. *Temperature- and strain rate-dependencies in compression. Only one strain rate has been experienced at 50°C. Decrease of the stress and increase of the strain rate influence as the temperature increases above 50°C.*

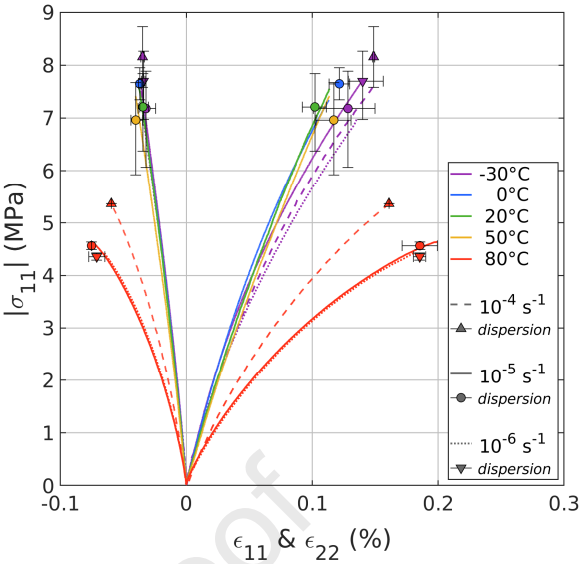

Figure 6. *Temperature- and strain rate-dependencies in tension. Only one strain rate has been experienced at 50°C. Decrease of the stress and increase of the strain rate influence as the temperature increases above 50°C.*

3.7. Cyclic loadings

Cyclic compression and tension loadings were performed on M2 (for cyclic tension data, see supplementary materials). The loading cycles had four phases: 1) load at a controlled strain rate, 2) stress relaxation at fixed longitudinal strain, 3) unload at a controlled strain rate, 4) strain recovery at rest. These tests are inspired by those performed on the material M1 (Gratton et al., 2009; Le et al., 2010). The experimental set-up was the same as for the monotonic tests. The relaxation and strain recovery lasted 8 hours, 1 hour and 10 minutes respectively for the uniaxial compression, the tension and the triaxial compression (Figure 7). Evolutions of stress and strain recorded during the relaxation and recovery parts of these experiments are plotted with respect to the time (see supplementary materials).

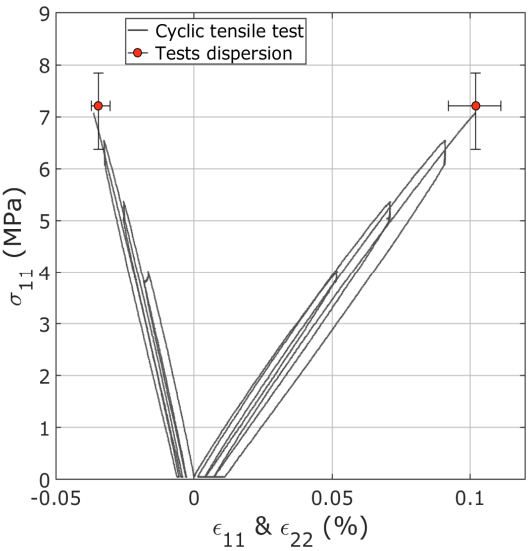

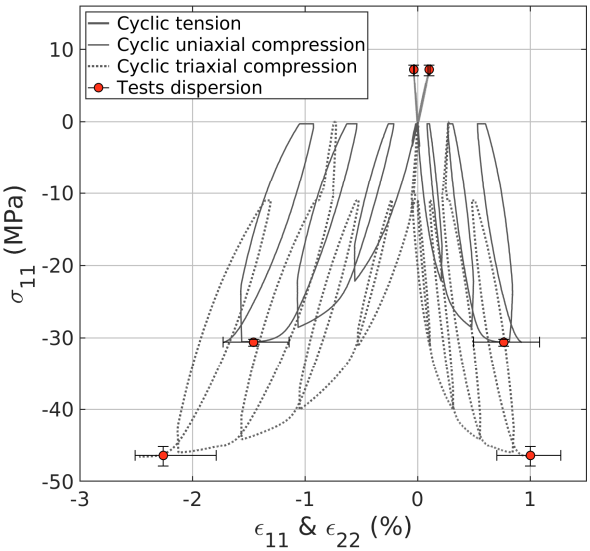

Figure 7*. Stress-strain curves for uniaxial tension (left), uniaxial compression (right, solid line; negative stress) and triaxial compression at 10 MPa pressure (right, dashed line; negative stress). This figure shows the pressure-dependence of the behavior.*

3.8. Double compression tests

An experimental campaign, inspired by Cambou and Lanier (Cambou and Lanier, 1988; Lanier et al., 1991) was carried out to highlight a possible loading-induced anisotropy, the latter being observed during a second loading in a different direction. Cubes with 20 mm sides were used. Here, only one bidirectional rosette was glued to the sample surface. The opposite side was covered with a pattern to perform a digital image correlation. The displacement rate was controlled by the mobile crosshead at 10^{-2} mm.s^{-1} corresponding to the reference strain rate up to a given stress. During the stress relaxation, the crosshead deforms even if its position (imposed at its ends) is fixed. This leads to an additional small compression of the sample. To avoid friction at the interfaces, lubricated Teflon was used. The displacement homogeneity was checked by digital image correlation.

First, the sample was compressed up to 30 MPa (0.95 times the maximum stress). After a one-hour relaxation, unloading and a night of recovery, the sample was submitted to a second compression, either in the same direction (test called "0°-0° compression"), or in an orthogonal direction by turning the cube (test called "0°-90° compression"). During this second loading, the sample was again compressed up to 30 MPa. Two representative tests (out of three of each kind) are illustrated in Figure 8 and Figure 9. The dispersion at the peak-stress of each cycle is also plotted. In these graphs, σ is the stress in the loading direction, ε_{11} (respectively ε_{22}) is the strain which is longitudinal (respectively transversal) during the first load.

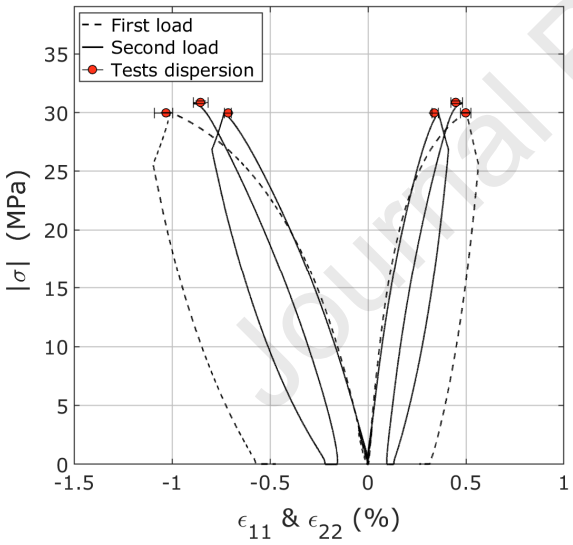

Figure 8*. Two compressions consecutively applied in the same direction (0°-0° compression). Strain set to zero at the beginning of the second load.*

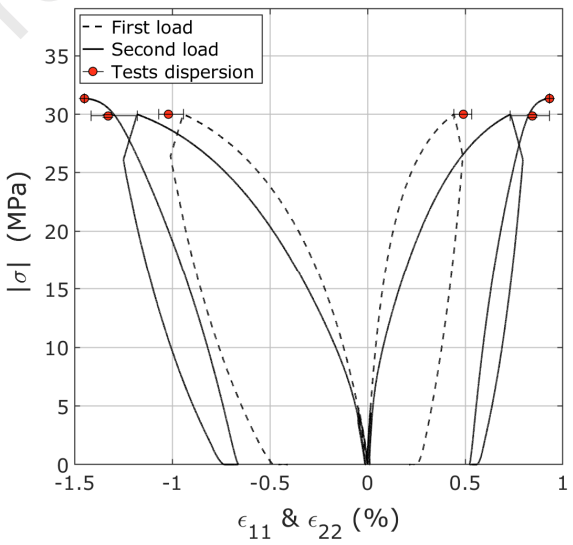

Figure 9. *Two compressions successively applied in two orthogonal directions (0°-90° compression). Strain set to zero at the beginning of the second load. Comparison with Fig. 8 shows the influence of the direction of the second loading.*

3.9. Fatigue test

The samples used were 20 mm high and 10 mm diameter cylinders. The loading rate was controlled by the crosshead at 0.025 mm.min^{-1}, which is approximately the reference strain rate. Two linear variable differential transformers (LVDT) were used to record the longitudinal strains of the specimen. The test was carried out with cycles between 1 and 30 MPa and until failure. The stress-strain curve – not reported here – shows the same hysteresis loop progressing on the strain axis for

each cycle. The evolution of the strain amplitude $\Delta\varepsilon_{11}$ between two consecutive cycles at the maximum stress (in red) and at the minimum stress (in blue) is given in Figure 10.

A repeated torsional cyclic test was also performed, using the same procedure as the monotonic test. The torsion cycles were applied between +8 MPa and -8 MPa. This test shows an immediate accommodation of the material, the second and twentieth hysteresis cycles being the same.

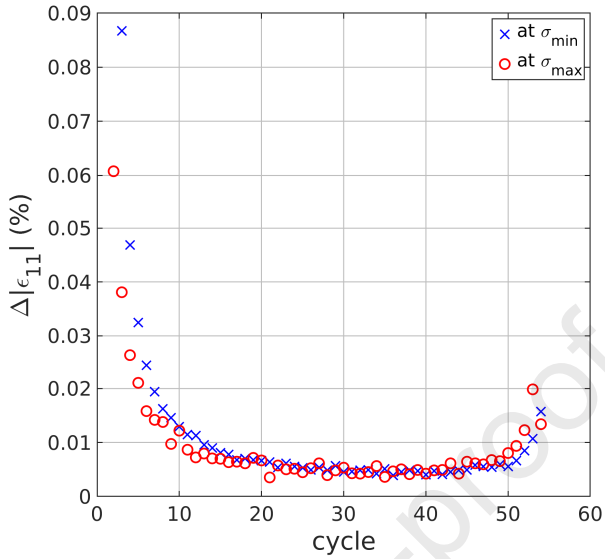

Figure 10. *Evolution of the strain amplitude $\Delta\varepsilon_{11}$, recorded between two consecutive σ_{min} (crosses) and σ_{max} (circles) of a compression fatigue test.*

3.10. Multiaxial failure tests

Three multiaxial tests were performed on M2: a Brazilian test, a channel-die test and an equibiaxial compression test.

For Brazilian tests, cylinders were compressed between two horizontal surfaces. The specimens were 15 mm diameter and 30 mm high cylinders. Latex 1.5 mm thick was placed on the interfaces to avoid a localized failure in the contact zone. A pattern was deposited on the circular surface of the cylinder to enable digital image correlation. The test was controlled by the displacement of the crosshead of the machine at a rate of 0.2 mm.min^{-1}. The specimen failed by traction along the transversal direction (centered and vertical macro-crack). The tension stress σ_1 and compressive stress σ_2 (at the center of the face) are estimated from the measured force F and the specimen dimensions as follows: $\sigma_1 = 2F/\pi\emptyset h$ and $\sigma_2 = -3\sigma_1$ (Picart and Pompon, 2016). The reader should be aware that the latter equations come from an elastic interpretation of the Brazilian test measurements, which could be discussed in light of the global behavior of M2.

A channel-die test is the compression of a cube for which one of the transversal directions is blocked. A picture of the set-up is given in Picart and Pompon (2016). The specimen used for these tests were a 20 mm-sided cubes whose faces were lubricated using 0.7 mm thick Teflon on the walls. The displacement field was measured by digital image correlation and a loading rate of 1.4x10^{-3} mm.s^{-1} (equivalent to a strain rate of about 3x10^{-5} s^{-1}) was applied using the crosshead. The longitudinal stress σ_2 is determined from the axial force applied to the sample. Since the transversal stress σ_1 is not measured, an estimation is proposed here using (1) the relation $\sigma_1=\upsilon\sigma_2$ and (2) a secant "Poisson's ratio" (here, the ratio of the transversal strain to the longitudinal) at failure of υ=0.5 as seen in Figure 3.

Equibiaxial compression tests were carried out on 20 mm-sided cubes (Figure 11). For the Brazilian and channel-die tests, the displacement field was measured by digital image correlation and the loading rate was controlled by the crosshead at 2.8x10^{-3} mm.s^{-1}, which is equivalent to about 1.5x10^{-5} s^{-1} in strain. 0.7 mm-thick Teflon, previously lubricated, was placed at the interfaces to limit friction. The main stresses are determined from the applied force F: $\sigma_1=\sigma_2=F/\sqrt{2}S$, with S the surface of a face of the cube.

The maximum principal stresses and strains recorded during these tests are given in Table 2.

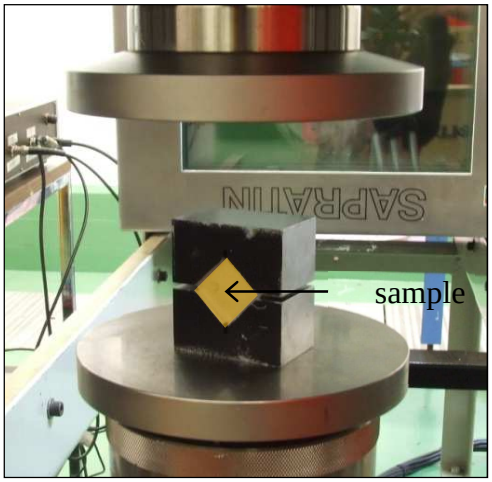

Figure 11. *Photograph of the equibiaxial compression test setup placed between the plates of the testing machine*.

Table 2. *Maximum principal stresses and strains recorded from the three tests. Data obtained using a model (elastic behavior or a secant "Poisson's ratio") are given in italics.*

	σ_1 (MPa)	σ_2 (MPa)	ε_1 (%)	ε_2 (%)
Brazilian test	*7.35 ±0.13*	*-22.07 ±0.23*	0.34 ± 0.07	-0.33 ± 0.11
Channel-die test	*-6.81 ±3.49*	-34.45 ± 0.57	0.50 ± 0.17	-1.50 ± 0.38
Equibiaxial compression	-32.57 ± 0.15	-32.57± 0.20	-0.68 ± 0.06	-0.62 ± 0.24

4. Main features of M2 behavior

The DMA measurements highlight a linear viscoelastic behavior verified using a displacement sweep study. Between 0°C and 60°C (reduced time lower than 6), the real modulus *E'* shows a slight decrease with an average value of about 8000 MPa and the imaginary modulus E'' reveals that the material is slightly viscous. From about 60°C, *E'* drops down to reach about 5000 MPa at 90°C, while *E''* reflects a significant material viscosity. However, this does not prove that viscoelasticity will remain linear at higher stress levels. Unfortunately, our Metravib apparatus does not allow us to investigate this question.

The comparison of the compression, tension and torsion curves (Figure 3) reveals a non-linear behavior and dependence on the loading direction. The tension and torsion curves show a brittle fracture at around 7.1 ±0.7 MPa in tension and 10.5 ±0.6 MPa in torsion. The compression shows increasing softening as the stress increases, until failure at 30.6 ±0.5 MPa. The compression failure is relatively more ductile but occurs at still low strains (1.50 ±0.2%). The asymmetry of the material behavior is highlighted. M2 is thus defined as a quasi-brittle material.

Let us note that, in torsion, the same maximum stress at failure is expected as for the tension test (failure in tension mode). An overestimation of the failure stress in torsion may result from a size effect: the effective area of a torsion sample is smaller than during a tension experiment, which decreases the probability of finding a defect (see for example Bazant and Planas, 1997). This effect has already been recorded on M1 and M2 when comparing data from tension test and three-point bend experiments (Picart and Pompon, 2016).

Figure 7 highlights a confinement-dependence of the material strength. Concerning the temperature-dependence, the material strength in compression (Figure 5) increases as the temperature decreases but there is little variation between 20°C and -30°C. In tension (Figure 6), a relative temperature-independence is noticed between -30°C and 50°C. At 80°C, in compression as in tension,

a more ductile behavior is observed, probably related to the glass transition of the explosive composition. Clear strain rate dependence is observed at 80°C. In the near future, some other tests will be made for a better description of the response of the material in the +50°C/+80°C thermal range.

The influence of loading conditions such as pressure, temperature, strain rate and stress sign on the Young's modulus and the Poisson's ratio is studied in detail. Since the curves do not show a clear transition to plasticity, an elastic longitudinal modulus is calculated by linear regression over a window of 0.05% longitudinal strain, while the Poisson's ratio is determined by the ratio of longitudinal and transversal strains at 0.05% longitudinal strain. The variations of the Young's modulus (respectively the Poisson's ratio) are given in Figure 12 and Figure 13 (respectively Figure 14 and Figure 15).

The Young's modulus appears to be independent of stress sign, strain rate, and temperature in the ranges from 0 to 10 MPa and between 0°C and 20°C. There is a slight decrease of the modulus at 50°C. At 80°C, it is halved, and its value increases with rate. The Poisson's ratio is independent of temperature, strain rate and stress sign on the range from 0°C to 80°C.

Let us discuss the observations made between 0°C and -30°C. From 0 to -30°C, DMA had shown a constant *E'* and a decrease of approximately 6-8% of *E'* after returning to 20°C. This observation is correlated on Figure 12 on the longitudinal modulus E_L. A linear extrapolation of data obtained between 0°C and 50°C yields E_L between 8500-9000 MPa (Figures 2 and 12) at -30°C when less than 8000 MPa was measured (Figure 12). This phenomenon is observed in both compression and tension modes. The Poisson's ratio also shows a curious evolution at the coldest temperature. Furthermore, a loss of linearity has been observed on M2 on its dilation coefficient under 0°C (decrease of the coefficient). This phenomenon seems different than the known ratchet-growth observed for PBX-9502 (Thompson et al., 2010) when the glass transition temperature of the material is crossed during thermal cycles. It could be attributed to "thermally activated damage" and possibly linked to the traction applied to the binder at the binder/grain interfaces. This damage was also observed on M1, for which glass transition is far less than for M2 (Picart and Brigolle, 2010). Since an in-depth analysis is required to determine the reasons of such an inelastic behavior, this phenomenon is beyond the scope of this paper.

The pressure-dependence of the elastic modulus is negligible since the values at 2.5, 5 and 10 MPa are included in the dispersion of the point at 0 MPa. This behavior is different from what Wiegand et al. (2011) and Picart et al. (2014) observed on two pressed HMX-based explosives. The pressure effect on Poisson's ratio is quite strange, showing a decrease of between 0 and 5 MPa in pressure before an increase for a 10 MPa confinement. The authors would like to point out that the phenomena (low modulus at 5 MPa) has been observed on other materials using different solid phase and binder (for an HMX-based PBX, see Benelfellah, 2013; Benelfellah et al., 2014, 2017 and Chatti, 2018; Chatti et al., 2017 on a mock material) and for experiments made by two different teams and set-ups. Further study of this point will be provided in future work.

The influence of loading conditions on stresses and strains at the peak have also been studied. Graphs can be found in the supplementary materials. The maximum tension stress is constant between -30°C and 50°C and decreases at 80°C. In compression, it regularly decreases between -30°C and 50°C and falls by half at 80°C. As for the Young's modulus, the strain rate influence is only observed at 80°C, for which the maximum stress increases with rate. Pressure increases the maximum stress, as is the case for granular materials. The maximum strains are constant while a slight increase is observed in compression in absolute values as the temperature rises. Furthermore, a small evolution of the maximum strains is recorded as the pressure rises. Temperature and pressure increase the peak-strain but not for the same reasons: the higher the temperature, the greater is the plastic flow of the material whereas the higher the pressure, the stronger is the material due to the internal friction.

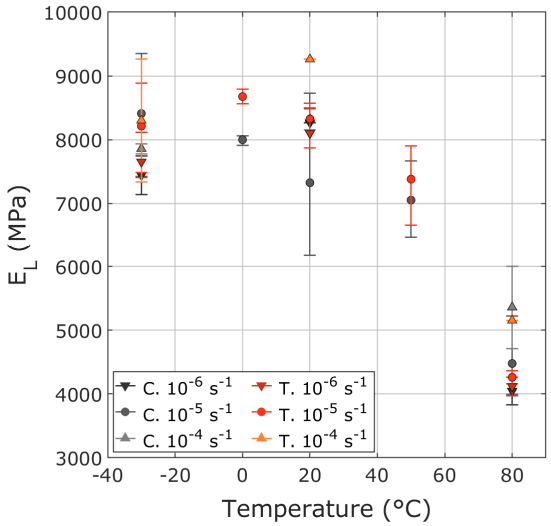

Figure 12. *Young's modulus in tension (in red) and compression (in grey) versus temperature for three strain rates at ambient pressure. A decrease is observed above 60°C.*

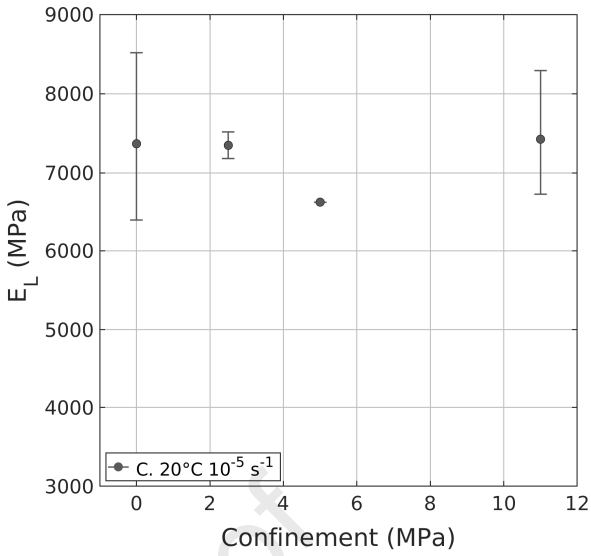

Figure 13. *Constant Young's modulus in compression versus confinement at a strain rate of 10^{-5} s^{-1} and ambient temperature.*

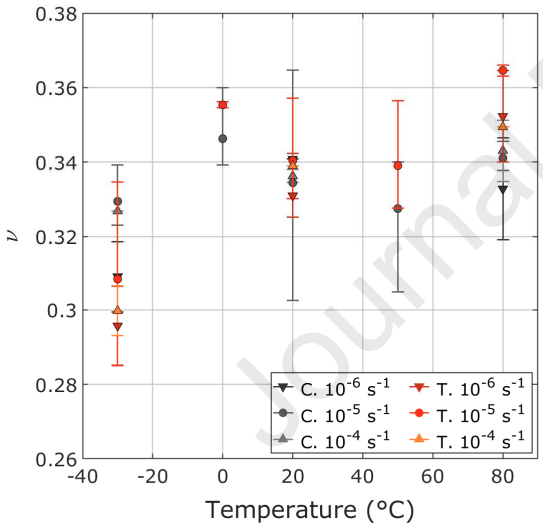

Figure 14*. Poisson's ratio in tension (in red) and compression (in grey) versus temperature for three strain rates at ambient pressure. Poisson's ratio is constant except a sudden decrease below 0°C.*

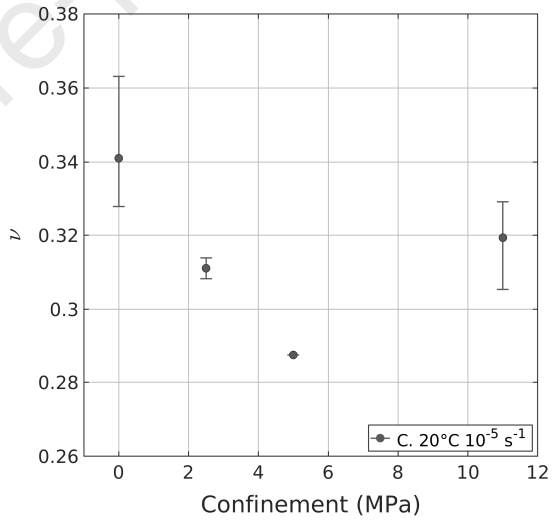

Figure 15. *Poisson's ratio in compression versus confinement at a strain rate of 10^{-5} s^{-1} and ambient temperature. A non-monotonic evolution (not explained) is observed as the pressure increases.*

An asymmetry between the tension and compressive responses is often observed for quasi-brittle granular materials (see Mazars et al., 1990 for concrete; Thomson et al., 2010 for PBX-9502; Buechler et al., 2012a for PBX-9501; and Picart et al., 2014 for M1). When these materials are submitted to alternating tension/compression loading, a stiffness recovery is observed at the beginning of compression (Mazars et al., 1990; Picart et al., 2014). This phenomenon is called unilateral effect and is classically related to damage. During the traction, cracks are created, the damage inducing a loss of stiffness. Then, during compression, these cracks close and a stiffness recovery is obtained. This interpretation also justifies that the material is more brittle in tension than in compression. For M2, the alternating tension/compression and compression/tension tests do not reveal any stiffness recovery when the sign of stress changes. However, it is possible that the material viscosity smooths the curves

and hides the phenomenon. The unilateral effect of M2 is in any case negligible compared to other strain mechanisms. Furthermore, it has been noticed that the failure point in tension and in compression is not influenced by the previous loading.

The cyclic tests carried out on M2 and shown in Figure 7 provide a lot of information on the mechanical behavior of the material. The relaxation and recovery steps enable the viscous effects to be removed. The strains at the end of the recovery step highlight the irreversible strains suffered by the material. Moreover, the comparison between the cyclic and monotonic curves shows that the cyclic test envelope corresponds to a monotonic test, so the addition of the cycles does not influence the overall behavior of M2. Assuming the stress state remains elastic during unloading, an elastic tangent modulus can be calculated at the beginning of each load and unload. They are determined by linear regression over a strain window of 0.05%. In doing so, constant moduli are observed during tension, uniaxial compression and triaxial compression tests (blue and red lines in Figure 16 for a uniaxial cyclic compression test). Consequently, damage is negligible on M2 up to 95% of the failure stress (peak-stress of the last cycle). Moreover, let us now suppose there is elastic unloading. Consequently, for each cycle, the secant modulus between the end of the relaxation and the end of the recovery is elastic (green lines in Figure 16). This assumption, made in previous papers (Gratton et al., 2009; Le et al., 2010; Picart et al., 2014) on M1, is commonly used for estimating the damage evolution of concrete (Benouniche, 1979; Gotuwka, 1999). Tangent and secant moduli are compared in Figure 16. The two methods give very different results: whereas tangent moduli (in blue and red) are constant, secant moduli (in green) decrease. Since the variations of the secant moduli cannot be imputed to damage, the observation demonstrates that some plasticity may develop during unloading. The same observations were made for cyclic compression under 10 MPa of confinement and cyclic tension, on both the longitudinal and the transversal strains. So, no induced anisotropic damage has been detected. However, theses cyclic tests highlight that the transversal strains grow faster than the longitudinal ones. Therefore, M2 develops a load-induced anisotropy.

The 0°-0° and 0°-90° compression tests have been performed to test the load-induced anisotropy of M2. To do this, the curves of the three kinds of loading of this campaign are compared in Figure 17, as conducted by Cambou and Lanier on Hostun sand (Cambou and Lanier, 1988). The strains are reinitialized at the beginning of each loading. The unloading curves are also shown in this graph. They have been inverted so that they read in the direction of their evolution and can be compared to the loadings curves. Figure 17 shows the first compression in red, the 0° reloading in blue, the 90° reloading in green and all the unloadings in grey. Since the strains are measured by only one gauge in each direction, the measured curves are more scattered than for the other experimental campaigns, the discrepancy being highlighted using a colored area.

Figure 17 shows different blue and green curves. One is stiffer than the initial compression (beyond 15 MPa), while the other is softer. The anisotropy induced by the first load is obvious. The direction of the sample which has undergone an expansion (the 90° direction, in green) is more ductile than initially. Conversely, the direction previously compressed (the 0° direction, in blue) is more rigid beyond a stress level of 15 MPa. This induced anisotropy cannot be attributed to damage since we have shown that this was negligible. This observation is confirmed by the fact that all the curves beginnings are superimposed: the elastic moduli have not been influenced by the first load. Furthermore, according to Figure 17, the unloading curves (in grey) are the same and match with the 0° reloading. It should also be noted that the 0° reloading (in blue) and the initial loading (in red) have overlapping areas up to 15 MPa. The same observations were made by Cambou and Lanier on a Hostun sand. The behavior of our material can be interpreted using a kinematic strain-hardening plasticity model, as described by the schemes in Figure 18. During a 0°-0° compression, the initial loading moves the plasticity surface up to 30 MPa. Then, the unloadings and the 0° reloading remain within this surface yielding an elastic response. During a 0°-90° compression, the initial loading moves the plasticity surface so that the yield strength decreases in the 90° direction. Thus, reloading at 90° yields more plasticity than during the first load. The plasticity surface is brought up to 30 MPa in the new direction, so the last unloading is then elastic.

To properly apply this interpretation to our case, the zero-stress point must stay within the plasticity surface, implying an initial yield stress higher than $\sigma_{max}/2$ = 15 MPa. If this condition is not satisfied, unloading at 90° would be different from the other unloading curves. However, the assumption of elastic unloading has been previously refuted. Nevertheless, if unloadings from cyclic compression of

cylindrical samples get some plastic flow, it may be possible that for cubes an artificial confinement induced an artificial increase of the yield stress even if the interfaces were lubricated.

The analysis of the compression, tension and torsion curves (Figure 3) shows that the behavior is non-linear starting from about 4 MPa. From the compression tests performed at 2.5, 5 and 10 MPa, the equivalent Von Mises yield stress is also about 4 MPa. These observations let us assume that the initial yield surface of M2 is a tube centered on the pressure axis, with a deviatoric 4 MPa radius. Furthermore, from the compression tests performed in temperature at various strain rates, non-linearity appears at about 4 MPa for tests at -30°C to 50°C, independently of the strain rate. At 80°C, the non-linearity appears from 2 MPa, whatever the strain rate. An in-depth study of the yield stress must be performed to complete these observations, but the initial plasticity criterion of M2 is independent of the pressure, the temperature up to the glass transition, and the strain rate.

For the fatigue test, the strain amplitude $\Delta\varepsilon_{11}$ between two cycles represented on Figure 10 rapidly decreases during the first twenty cycles before becoming constant. A few cycles before failure, a rapid increase of $\Delta\varepsilon_{11}$ is observed. These observations can be interpreted by assuming that two mechanisms with opposite effects add up: a plastic accommodation yielding a decrease of the strain amplitude and late damage which will increase the strain amplitude. The plastic accommodation – also called ratchetting effect – can be modelled by a combined kinematic-isotropic hardening. Furthermore, let us recall that the torsion fatigue test with zero mean stress has shown an immediate accommodation of the material. This phenomenon should be taken into account for the hardening modelling.

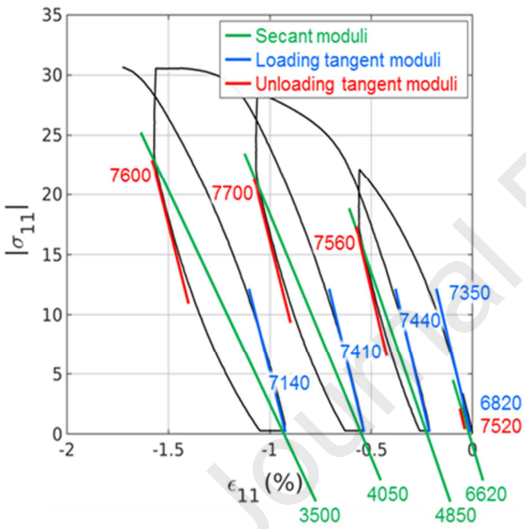

***Figure 16**. Secant and tangent longitudinal moduli for a cyclic compression test. Secant moduli decrease is interpreted as a damage effect when the tangent moduli do not show any evolution.*

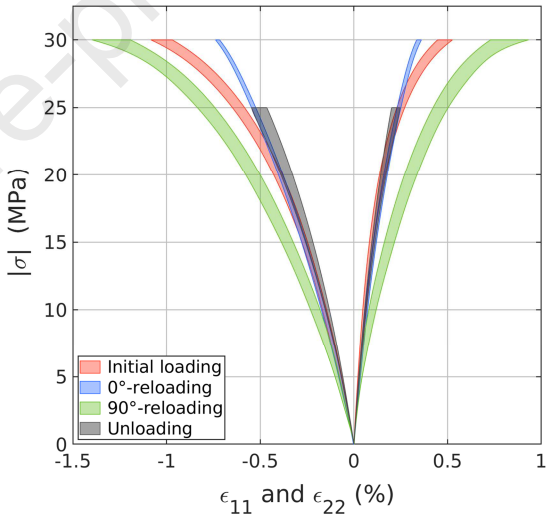

***Figure 17.** Comparison of the loading and unloading curves of the 0°-0° and 0°-90° tests. The response depends on the reloading direction highlighting an induced-anisotropic during the first loading.*

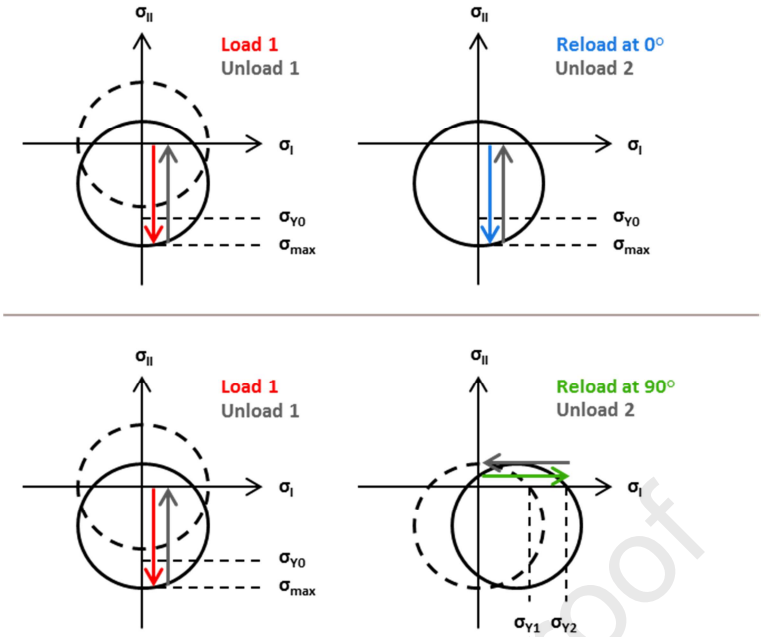

Figure 18. *Sketch illustrating the material response during the 0°-0° (top) and 0°-90° (bottom) compressions by a kinematic strain-hardening plasticity model. The displacement of the yield surface due to the first load induces a different response depending on the reloading direction.*

From the longitudinal strain ε_{11} and transversal strain ε_{22} measured during uniaxial compression and tension tests, the volumetric strains ε_V and deviatoric strains ε_D can be plotted with respect to the mean stress P and the equivalent Von Mises stress Q:

$$\begin{cases} \varepsilon_V = \varepsilon_{11} + 2\,\varepsilon_{22} \\ \varepsilon_D = |\,\varepsilon_{11} - \varepsilon_{22}\,| \end{cases} \quad \text{and} \quad \begin{cases} P = \dfrac{1}{3}\mathrm{tr}\left(\underline{\underline{\sigma}}\right) = \dfrac{\sigma_{11}}{3} + \sigma_{22} \\ Q = \sqrt{\dfrac{3}{2}\,\underline{\underline{\sigma_D}} : \underline{\underline{\sigma_D}}} = |\sigma_{11} - \sigma_{22}| \end{cases} \tag{2}$$

The volumetric curves of the compression tests at various strain rates, temperatures and pressures (Figure 19 and Figure 23) show an almost linear compacting behavior up to a stress level of about 70% to 90% of the peak stress. Beyond that, the material develops a dilatant behavior, which reflects a rapid increase of the transversal strains compared to the longitudinal ones. This dilatancy is often attributed to anisotropic damage (see what is done in the concrete community for example), but this interpretation is not possible for M2 since the damage independence has been highlighted under these stress levels (no variation of elastic moduli). The simplest interpretation is to attribute this phenomenon to a volumetric plastic flow, as this is often the case for geomaterials, for example [36].

For tension tests, while the deviatoric behavior is temperature-independent between -30°C and 50°C (Figure 22), the volumetric behavior reveals temperature dependence (Figure 21). Given the measurement dispersion, the tests performed at 20°C and 50°C can be considered as identical, but the tests at 0°C and -30°C show some differences. The colder the temperature, the more the non-linearity of the stress - volumetric strain curve increases, leading to higher failure strains. This phenomenon correlates the observations in DMA, which suggest the existence of thermal isotropic damage. Moreover, according to the dispersion and the curves ordering, there is no strain rate effect at -30°C in tension. The 20°C curves at 10^{-6} s^{-1} and 10^{-4} s^{-1} are close to the curve recorded at 10^{-5} s^{-1}, and thus not shown.

The deviatoric behavior (Figure 20, Figure 22 and Figure 24) seems to be independent of strain rate, temperature between -30°C and 50°C, pressure and stress sign up to an equivalent stress of about 10 to 15 MPa. For compression tests (Figure 20 and Figure 24), a pronounced non-linearity appears beyond this, tending towards an asymptotic behavior. By imputing these volumetric and deviatoric behaviors to the plastic flow, this would point to a non-linear strain-hardening.

Figure 21 shows more flexible behavior at -30 and +80°C than the mild temperature response. The measurement made at +80°C could be related to the decrease of the viscosity of the material with the

temperature as in Figures 19, 20 and 22. At -30°C, the DMA measurements point to "damage" thermally activated below 0°C. This "damage" has a negligible influence during compressive loading when its influence is enhanced for tension loadings. More in-depth study is needed to identify its causes.

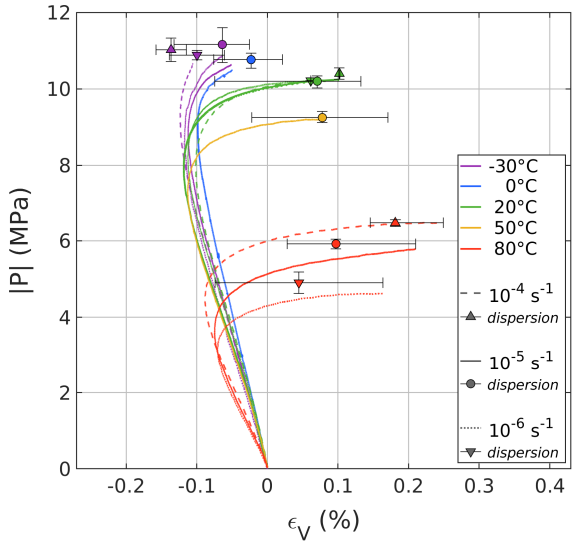

Figure 19. *Mean stress evolution with volumetric strain for simple compression tests performed between -30°C and 80°C for three strain rates. Whatever the loading conditions, a compaction is first followed by a positive volume change.*

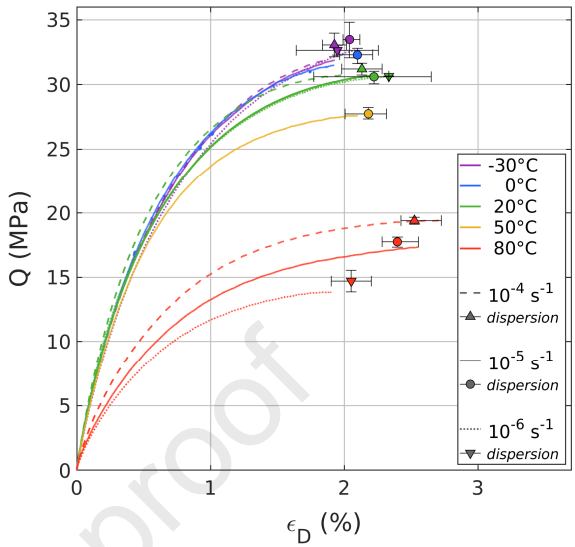

Figure 20. *Equivalent stress evolution with deviatoric strain for simple compression tests performed between -30°C and 80°C for three strain rates.*

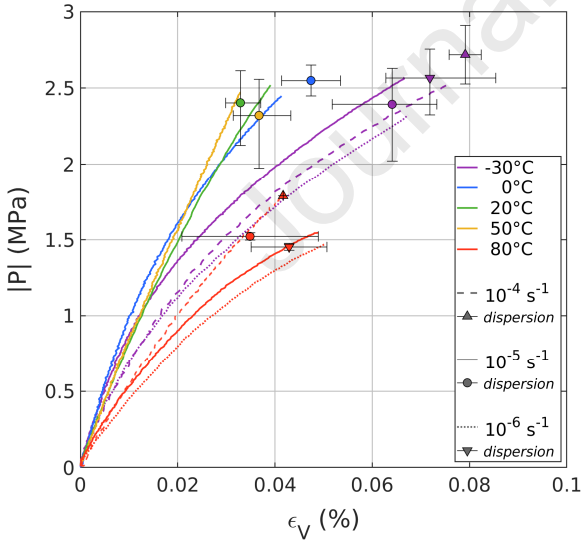

Figure 21. *Mean stress evolution with volumetric strain for simple tension tests performed between -30°C and 80°C for three strain rates. Whatever the loading conditions, the volume of the sample increases.*

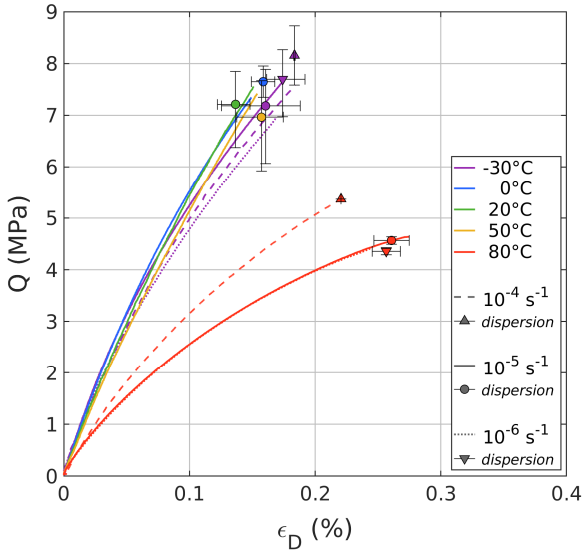

Figure 22. *Equivalent stress evolution with deviatoric strain for simple tension tests performed between -30°C and 80°C for three strain rates.*

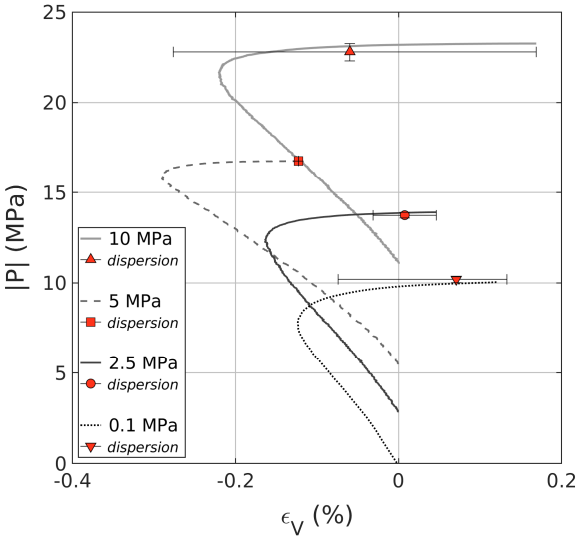

Figure 23. *Mean stress evolution with volumetric strain for triaxial compression tests performed between 0.1 and 10 MPa at a strain rate of 10^{-5} s^{-1}. Compaction is first observed followed by a positive volume change.*

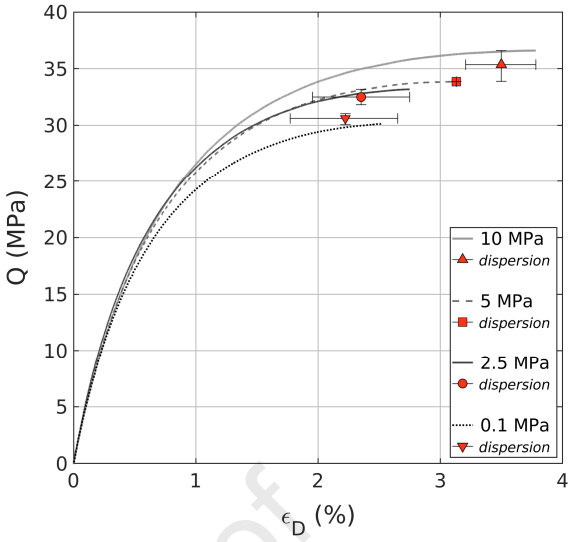

Figure 24. *Equivalent stress evolution with deviatoric strain for triaxial compression tests performed between 0.1 and 10 MPa at a strain rate of 10^{-5} s^{-1}.*

For the tests with the third principal stress as null, the M2 failure points can be represented in the principal stress plane (σ_1;σ_2), as Picart and Pompon (2016) have done for the material M1. This indicates that the failure criterion developed for M1 could potentially be adapted to M2 (see Table 2).

5. Guidelines for model improvement

The experimental data on HMX- and TATB-based PBXs have been summarized in Table 1 and in sections 3 and 4 of M2. HMX- and TATB-based PBXs are made of a very high solid fraction of organic crystals. If the behaviors of the TATB and HMX crystals differ (anisotropy, elastic constants, etc.), the stiffnesses of the latter remain of the same order of magnitude. Adding a few percentage of a polymeric binder gives different viscous responses for the explosive compositions. For pressed PBXs studied here, the residual porosity is of the same order (a few percent) and the Young's moduli, the Poisson's ratios and the maximum stresses (and associated strains) are comparable. As an example, in uniaxial compression or tension loadings, the peak stresses and the strain differ by a factor of 2 only. Therefore, in the authors' opinion, a "unified constitutive law" could be proposed for this class of materials, taking into account an in-depth characterization of the behavior. If mechanisms implemented in this future law could be the same, each explosive composition would have its own set of parameters, like the von Mises threshold for metals and the different initial yield stresses depending on the materials.

The aim of this section is to provide guidelines to model improvement. A constitutive law for the state of the art is first proposed, highlighting data used to calibrate or validate each model. There then follows a discussion, to determine what future work needs to be done.

The following nomenclature is adopted for splitting the stress $\underline{\underline{\sigma}}$ and strain $\underline{\underline{\varepsilon}}$ tensors into mean (denoted $.^V$) and deviatoric (denoted $.^D$) parts using the second order unit tensor $\underline{\underline{1}}$: $\sigma^V=\mathrm{tr}\left(\underline{\underline{\sigma}}\right)/3$ and $\underline{\underline{\sigma}}^D=\underline{\underline{\sigma}}-\sigma^V\underline{\underline{1}}$; $\varepsilon^V=\mathrm{tr}\left(\underline{\underline{\varepsilon}}\right)$ and $\underline{\underline{\varepsilon}}^D=\underline{\underline{\varepsilon}}-\frac{1}{3}\varepsilon^V\underline{\underline{1}}$.

5.1. SCRAM model

The SCRAM model, sketched by Dienes in 1978 (Dienes, 1978), is particularly well-detailed in a 2006 paper (Dienes et al., 2006). This model was developed in order to understand anomalous behavior of some energetic materials: low-speed impact can lead to violent reactions in a seemingly random and unpredictable way. The commonly accepted theory is that a low-speed impact can involve the formation and coalescence of hotspots, which can lead to a deflagration or a detonation. The SCRAM model links damage to the formation of hotspots and the initiation (thermal explosion) of the explosive. For the present study, we are interested in the quasistatic declination of this model. The theory is based on the strain rates additivity at the macroscopic scale. The deformation mechanisms are as follows: matrix elasticity; anisotropic crack nucleation, growth and coalescence; friction of shear-closed cracks; and plasticity. The model is written, in small strains, from the addition of the strain rates:

$$\underline{\underline{\dot{\varepsilon}}}_{tot} = \underline{\underline{\dot{\varepsilon}}}_{el} + \underline{\underline{\dot{\varepsilon}}}_{pl} + \underline{\underline{\dot{\varepsilon}}}_{c} + \underline{\underline{\dot{\varepsilon}}}_{g} \tag{3}$$

where $\underline{\underline{\dot{\varepsilon}}}_{tot}$ is the total strain rate, $\underline{\underline{\dot{\varepsilon}}}_{el}$ the matrix elasticity, $\underline{\underline{\dot{\varepsilon}}}_{pl}$ the matrix plastic flow, $\underline{\underline{\dot{\varepsilon}}}_{c}$ the microcracks opening and shearing, and $\underline{\underline{\dot{\varepsilon}}}_{g}$ the microcracks growth and coalescence. The elastic contribution is defined by Hooke's law. The plastic response of the material is described by a deviatoric linear kinematic hardening and an associated flow. The model takes the following general form:

$$\underline{\underline{\dot{\sigma}}} = \left(\underline{\underline{\underline{\underline{\mathbb{C}}}}}^{-1} + \underline{\underline{\underline{\underline{\mathcal{F}}}}}_{c} \right)^{-1} : \left(\underline{\underline{\dot{\varepsilon}}}_{tot} - \underline{\underline{\underline{\underline{\mathcal{F}}}}}_{g} : \underline{\underline{\sigma}} - \dot{\lambda} \frac{\underline{\underline{\sigma}}^{D} - \underline{\underline{X}}^{D}}{\sqrt{\left(\underline{\underline{\sigma}}^{D} - \underline{\underline{X}}^{D}\right) : \left(\underline{\underline{\sigma}}^{D} - \underline{\underline{X}}^{D}\right)}} \right) \tag{4}$$

where $\underline{\underline{\sigma}}$ is the global stress tensor and $\underline{\underline{\underline{\underline{\mathbb{C}}}}}$ is the elastic stiffness matrix. $\underline{\underline{X}}^{D}$ is the deviatoric kinematic hardening tensor and $\dot{\lambda}$ is the plastic multiplier. The plasticity criterion is written as follows (σ_Y is the initial yield stress):

$$f = \left(\underline{\underline{\sigma}}^{D} - \underline{\underline{X}}^{D}\right) : \left(\underline{\underline{\sigma}}^{D} - \underline{\underline{X}}^{D}\right) - \sigma_Y^2 \tag{5}$$

The 4th-order tensors $\underline{\underline{\underline{\underline{\mathcal{F}}}}}_{c}$ and $\underline{\underline{\underline{\underline{\mathcal{F}}}}}_{g}$ respectively refer to crack opening/shearing and to crack growth. The solid angle associated with the hemisphere is discretized into $\Delta\psi$. This corresponds to the sum of the contributions of each crack network defined by its normal (vector $\underline{n}$) orienting the solid angle portion $\Delta\psi$.

$$\underline{\underline{\underline{\underline{\mathcal{F}}}}}_{c} = \beta \sum_{\substack{\text{hemi-}\\ \text{sphere}}} F(\underline{n}) \left(H(\sigma_n)\, \underline{\underline{\underline{\underline{C}}}}^{o}(\underline{n}) + H(-\sigma_n) \langle 1-\eta(\underline{n}) \rangle \underline{\underline{\underline{\underline{C}}}}^{s}(\underline{n}) \right) \Delta\psi \tag{6}$$

$$\underline{\underline{\underline{\underline{\mathcal{F}}}}}_{g} = \beta \sum_{\substack{\text{hemi-}\\ \text{sphere}}} \dot{F}(\underline{n}) \left(H(\sigma_n)\, \underline{\underline{\underline{\underline{C}}}}^{o}(\underline{n}) + H(-\sigma_n) \langle 1-\eta(\underline{n}) \rangle \underline{\underline{\underline{\underline{C}}}}^{s}(\underline{n}) \right) \Delta\psi \tag{7}$$

where $H(\sigma_n)$ is the Heaviside function of the normal stress $\sigma_n = \underline{n}\ \underline{\underline{\sigma}}\ \underline{n}$. $H(\sigma_n)$ is zero for opened microcracks and one for closed microcracks. The term $\langle 1-\eta(\underline{n}) \rangle$, with $\langle\ .\ \rangle$ denoting the Macaulay brackets, corresponds to the microcrack sliding criterion: this term is equal to zero when the crack is blocked (no shear) and is one when it is sliding-free. The coefficient η is defined from the friction state of the family of cracks oriented by $\underline{n}$ and the friction coefficient μ: $\eta = \frac{\mu \langle -\sigma_n \rangle}{s_n}$, with $s_n = \sqrt{\underline{n}\ \underline{\underline{\sigma}}\ \underline{\underline{\sigma}}\ \underline{n} - \sigma_n^2}$. Thus, whereas the pressure is not involved in the plasticity criterion, damage evolution and effectivity (defined as how the damage of a given network does or does not affect the behavior depending on the loading direction) as well as frictional sliding are pressure-dependent since they depend on the sign of σ_n. The tensors $\underline{\underline{\underline{\underline{C}}}}^{o}(\underline{n})$ and $\underline{\underline{\underline{\underline{C}}}}^{s}(\underline{n})$ of equation (4) describe the opening and shearing directions of the microcrack. β [MPa^{-1}] is a constant coming from analytic solutions for penny-shaped cracks. The

function $F(\underline{n}) = \int_0^\infty n(c,\underline{n})\, c^3\, dc$ describes the crack distribution, with $n(c,\underline{n})$ representing the distribution of the microcracks of length c and normal vector $\underline{n}$. The crack growth rate $\dot{c}$ is controlled by the rate of dissipated energy $g\left(\underline{\underline{\sigma}},\underline{n},c\right)$:

$$\begin{cases} \dot{c}\left(\underline{\underline{\sigma}},\underline{n},c\right) = \dot{c}_{max}\dfrac{1}{1+m}\left(\dfrac{g\left(\underline{\underline{\sigma}},\underline{n},c\right)}{\left(1+\dfrac{1}{m}\right)g_c}\right)^m & \text{if } g\left(\underline{\underline{\sigma}},\underline{n},c\right) \le \left(1+\dfrac{1}{m}\right)g_c \\ \dot{c}\left(\underline{\underline{\sigma}},\underline{n},c\right) = \dot{c}_{max}\left(1 - \dfrac{g_c}{g\left(\underline{\underline{\sigma}},\underline{n},c\right)}\right) & \text{if } g\left(\underline{\underline{\sigma}},\underline{n},c\right) \ge \left(1+\dfrac{1}{m}\right)g_c \end{cases} \tag{8}$$

where m is an exponent greater than one. In this model, the maximum crack growth rate $\dot{c}_{max}$ is assumed to have the magnitude of the Rayleigh wave speed and g_c is the critical rate of dissipated energy. The function g is written as follows:

$$g\left(\underline{\underline{\sigma}},\underline{n},c\right) = \frac{4}{\pi}\frac{1-\nu}{1-\frac{\nu}{2}}\frac{c}{2G}\left(H(\sigma_n)\left(\left(1-\frac{\nu}{2}\right)\sigma_n^{\,2} + s_n^{\,2}\right) + H(-\sigma_n)\,\langle\, \mu\sigma_n + s_n \,\rangle\right) \tag{9}$$

where ν and G are respectively the Poisson's ratio and the shear modulus.

It can be seen that g – and so $\dot{c}$ – is greater in tension (σ_n positive) than in compression (σ_n negative). In addition, for a closed microcrack (σ_n negative) whose frictional sliding is blocked (factor $\langle 1\text{-}\eta \rangle$ null): $\eta \le 1 \Longrightarrow s_n \le \mu\sigma_n \Longrightarrow g=0 \Longrightarrow \dot{c}=0$; the microcrack cannot grow. Apart from this particular case, as soon as the stress state of a microcrack is not zero, it expands.

The mechanical parameters of this model are determined for PBX-9501 from only one monotonic uniaxial compression test performed at 10^{-2} s^{-1} without transversal strain measurements. The fit of the parameters is not detailed. The validation of SCRAM on the quasistatic domain is missing. Dienes compares the simulation, calibrated on a compression at 10^{-2} s^{-1}, to experimental compression performed at $2x10^{-2}$ s^{-1}, the rate effect between these two tests being negligible (both experimentally and numerically).

5.2. ViscoSCRAM model (VS)

The ViscoSCRAM model defined in (Bennett et al., in 1998) puts the deviatoric component of the IsoSCRAM model proposed by Addessio and Johnson (1990) for quasi-brittle materials in series with a generalized Maxwell model with N branches. The volumetric component of the model is described by a linear elastic law. The total strain rate is split into volumetric and deviatoric components. From the additivity of the viscoelastic and the crack growth strain rates (plasticity of the matrix is ignored), the ViscoSCRAM model is written as follows:

$$\begin{cases} \dot{\sigma}^V = K\,\dot{\varepsilon}_{tot}{}^V \\ \underline{\dot{\sigma}}^D = \dfrac{2G\,\underline{\underline{\dot{\varepsilon}}}_{tot}{}^D - \sum_{b=1}^{N}\dfrac{\underline{\underline{\sigma_b}}^D}{\tau_b} - 3\left(\dfrac{c}{a}\right)^2\dfrac{\dot{c}}{a}\,\underline{\sigma}^D}{1+\left(\dfrac{c}{a}\right)^3} \end{cases} \tag{10}$$

$\underline{\sigma}^D$ is the total deviatoric stress, corresponding to the sum of the stress $\underline{\underline{\sigma_b}}^D$ of each branch. K is the bulk elastic modulus. G is the sum of the shear moduli of the N branches. τ_b is the characteristic time of the b^{th} branch. The constant a is the average initial porosity size. Compared to SCRAM, the crack growth rate $\dot{c}$ is largely simplified by the assumption of isotropic damage:

$$\begin{cases} \dot{c}\left(\underline{\underline{\sigma}}^{D},c\right) = \dot{c}_{max}\,\dfrac{1}{1+\dfrac{m}{2}}\left(\dfrac{\mathrm{J}\left(\underline{\underline{\sigma}}^{\mathrm{D}},c\right)}{\sqrt{1+\dfrac{2}{m}}J_0}\right)^{m} & \text{if } \mathrm{J}\left(\underline{\underline{\sigma}}^{\mathrm{D}},c\right) \le J_0\sqrt{1+\dfrac{2}{m}} \\ \dot{c}\left(\underline{\underline{\sigma}}^{\mathrm{D}},c\right) = \dot{c}_{max}\left(1 - \dfrac{{J_0}^2}{\mathrm{J}\left(\underline{\underline{\sigma}}^{\mathrm{D}},c\right)^2}\right) & \text{if } \mathrm{J}\left(\underline{\underline{\sigma}}^{\mathrm{D}},c\right) \ge J_0\sqrt{1+\dfrac{2}{m}} \end{cases} \tag{11}$$

where J_0 is a parameter (in $\mathrm{Pa}\sqrt{m}$). The function J is written according to Hackett and Bennett (2000):

$$\mathrm{J}\left(\underline{\underline{\sigma}}^{D},c\right) = \sqrt{\frac{3}{2}\pi c\;\underline{\underline{\sigma}}^{\mathrm{D}}:\underline{\underline{\sigma}}^{\mathrm{D}}} \tag{12}$$

With this formulation, the crack growth rate ċ depends only on the deviatoric stress and therefore is pressure-independent, unlike in the SCRAM model (previous equations (8) and (9)).

The model calibration is performed for PBX-9501 (Bennett et al., 1998). The shear moduli of the five viscoelastic branches (to cover different strain rates) are determined from the Young's modulus from four compressions in the quasistatic range and two at high strain rates, and an assumed Poisson's ratio of 0.3. The determination of the parameters J_0, a and m is not detailed.

In the quasistatic range, Hackett and Bennett (2000) have compared ViscoSCRAM to a three-point bending test on PBX-9501, the model predicting the experimental force-displacement curves. Later, Rangaswamy et al. (2010) have simulated a Brazilian test. The quasi-linear part of the experimental curves is reproduced but the simulated displacement deviates from the measurements before reaching the maximum stress. The horizontal strain field from the finite element simulation is compared with experimental digital image correlation. The strains at the macrocrack boundary are largely underestimated.

5.3. ViscoSCRAM viscoplastic model (VS-VP)

Liu and coworkers (Liu et al., 2019) recently proposed a modified version of ViscoSCRAM by adding a deviatoric viscoplasticity (Bodner, 1987) in series with the original model, resulting in the following expressions:

$$\begin{cases} \dot{\sigma}^{V} = K\,\dot{\varepsilon}_{tot}{}^{V} \\ \underline{\underline{\dot{\sigma}}}^{D} = \dfrac{2G\;\underline{\underline{\dot{\varepsilon}}}_{\mathrm{tot}}{}^{D} - \sum_{b=1}^{N}\dfrac{\underline{\underline{\sigma_b}}^{\mathrm{D}}}{\tau_b} - \left(3\left(\dfrac{c}{a}\right)^2\dfrac{\dot{c}}{a} + \dot{\lambda}\dfrac{2\mathrm{G}}{\sqrt{\dfrac{2}{3}\,\underline{\underline{\sigma}}^{\mathrm{D}}:\underline{\underline{\sigma}}^{\mathrm{D}}}}\right)\underline{\underline{\sigma}}^{\mathrm{D}}}{1+\left(\dfrac{c}{a}\right)^3} \end{cases} \tag{13}$$

An isotropic hardening is computed from an upper limit weighted by a function of the ratio of deviatoric stress and plastic work, and not from a stress yield criterion with hardening. A viscoplastic strain rate always exists in this model.

The crack growth ċ is taken from Buechler and Luscher (Buechler and Luscher, 2014) to introduce pressure dependence and tension–compression asymmetry as follows:

$$\begin{cases} \dot{c}\left(\underline{\underline{\sigma}},c\right) = \dot{c}_{res}\,\dfrac{1}{1+\dfrac{m}{2}}\left(\dfrac{\mathrm{J}\left(\underline{\underline{\sigma}},c\right)}{\mathrm{J}_{0\mu}(\sigma^{V},c)\sqrt{1+\dfrac{2}{m}}}\right)^{m} & \text{if } \mathrm{J}\left(\underline{\underline{\sigma}},c\right) \le \mathrm{J}_{0\mu}(\sigma^{V},c)\sqrt{1+\dfrac{2}{m}} \\ \dot{c}\left(\underline{\underline{\sigma}},c\right) = \dot{c}_{res}\left(1 - \dfrac{\mathrm{J}_{0\mu}(\sigma^{V},c)^2}{\mathrm{J}\left(\underline{\underline{\sigma}},c\right)^2}\right) & \text{if } \mathrm{J}\left(\underline{\underline{\sigma}},c\right) \ge \mathrm{J}_{0\mu}(\sigma^{V},c)\sqrt{1+\dfrac{2}{m}} \end{cases} \tag{14}$$

Compared to the original ViscoSCRAM model (equation (11)), the speed $\dot{c}_{max}$ is replaced by $\dot{c}_{res}$ which is a logarithmic function of the strain rate, bounded by the Rayleigh wave speed. The function J depends on the pressure σ^V, and the constant J_0 is multiplied by a factor depending on pressure, crack length and dynamic friction coefficient μ', resulting in $J_{0\mu}$.

$$J\left(\underline{\underline{\sigma}},c\right) = \sqrt{\pi c}\left(H(\sigma^V)\sqrt{\frac{3}{2}\left(\underline{\underline{\sigma}}^D:\underline{\underline{\sigma}}^D + 3\sigma^{V\,2}\right)} + H(-\sigma^V)\sqrt{\frac{3}{2}\,\underline{\underline{\sigma}}^D:\underline{\underline{\sigma}}^D}\right) \tag{15}$$

$$J_{0\mu}(\sigma^V,c) = J_0\sqrt{1 - \pi\,\frac{\mu'\sqrt{c}\,\sigma^V}{J_0}\left(1-\frac{\mu'\sqrt{c}\,\sigma^V}{J_0}\right)} \tag{16}$$

With this formulation, J is greater in tension (σ^V positive) than in compression (σ^V negative) while the function $J_{0\mu}$ is lower in tension than in compression. Thus, the ratio $J/J_{0\mu}$ and so the growth rate $\dot{c}$ is higher in tension than in compression. As in SCRAM, an opened crack grows faster than a closed one.

There are 19 parameters fitted on the longitudinal strains of monotonic tension and compression tests performed at 50°C and 10^{-4} s^{-1} on a PBX-9502 sample (Thompson et al., 2010), and secondly another set of parameters calibrated on a cyclic compression test performed on M2 using the curves taken from Ambos et al. (2015) and Gasnier et al. (2018). From these calibrations, all this results in the maximum strains in tension being underestimated by half. Furthermore, the unloading and reloading steps do not get any hysteresis.

In order to validate the model, Liu et al. (2019) have simulated a compression of a perforated plate of PBX-9502 (Liu and Thompson, 2014), and they compare the experimental and simulated force-displacement curves. The two plots coincide up to the maximum stress. The experimental horizontal strain field from digital image correlation is also compared to a finite element simulation. Although the shape is accurately reproduced, the displacement calculated around the hole is less significant than the measurements. The authors did not provide a comparison for vertical strains, for which experimental data are however available (Liu and Thompson, 2014).

5.4. Viscoelastic plastic model (VE-P)

The research carried out on M1 and M2 has led to several constitutive laws being developed from a substantial experimental base (see section 2). For material M1, a model describing a non-linear viscoelasticity with pressure and temperature dependencies was established in the 1980s (Belmas et al., 1982). Since this approach only enables simulation of monotonic tests, we refer the reader to the original paper for its description. A second model was proposed by Gratton et al. (2009), including an elasto-viscoplastic law with isotropic damage and pressure-dependent viscoplastic behavior. This model was later completed to describe the viscoelasticity visible during load-unload loops. In 2010, Le and coworkers (Le et al., 2010) proposed a viscoelastic-plastic constitutive law for M1 including isotropic damage. This model is based on a generalized Maxwell model in which one of the branches – numbered 0 – is elastoplastic. The other branches are viscoelastic. All the elastic moduli are identically damaged. The parabolic plasticity criterion is defined from the mean and deviatoric stresses of the elastoplastic branch with an isotropic strain-hardening:

$$f = \sqrt{\frac{1}{3}\,\underline{\underline{\sigma_0}}^D:\underline{\underline{\sigma_0}}^D + \frac{k^2}{R(k)}\,\sigma_0{}^V} - k \tag{17}$$

The isotropic hardening variables k and $R(k)$ are related to the cumulative plastic strain $\overline{\varepsilon_{pl}}$. A non-associated plastic flow is empirically determined, involving a dilatancy coefficient β^* which controls the volumetric to deviatoric plastic strain ratio:

$$\begin{cases} \dot{\varepsilon}_{pl}{}^V = \dot{\lambda}\,\dfrac{\beta^*}{\sqrt{3\left(1+\beta^{*2}\right)}} \\ \underline{\underline{\dot{\varepsilon}_{pl}}}^D = \dot{\lambda}\,\dfrac{1}{\sqrt{1+\beta^{*2}}}\,\dfrac{\underline{\underline{\sigma_0}}^D}{\sqrt{\underline{\underline{\sigma_0}}^D:\underline{\underline{\sigma_0}}^D}} \end{cases} \tag{18}$$

The elastoplastic stress, $\underline{\underline{\sigma_0}}$, and the viscoelastic stresses, $\underline{\underline{\sigma_b}}$, add up to give the global stress, leading to the following form of the model:

$$\begin{cases} \dot{\sigma}^V = K(1\text{-}d)\ \dot{\varepsilon}_{tot}{}^V - \sum_{b=1}^{N} \dfrac{\sigma_b{}^V}{\tau_b} - \dfrac{\dot{d}}{1\text{-}d}\ \sigma^V - K_0\left((1\text{-}d)\ \dot{\varepsilon}_{pl}{}^V - \dot{d}\left(\varepsilon_{tot}{}^V\text{-}\varepsilon_{pl}{}^V\right)\right) \\ \underline{\underline{\dot{\sigma}}}^D = 2G(1\text{-}d)\ \underline{\underline{\dot{\varepsilon}_{tot}}}^D - \sum_{b=1}^{N} \dfrac{\underline{\underline{\sigma_b}}^D}{\tau_b} - \dfrac{\dot{d}}{1\text{-}d}\ \underline{\underline{\sigma}}^D - 2G_0\left((1\text{-}d)\ \underline{\underline{\dot{\varepsilon}_{pl}}}^D - \dot{d}\left(\underline{\underline{\varepsilon_{tot}}}^D\text{-}\underline{\underline{\varepsilon_{pl}}}^D\right)\right) \end{cases} \quad (19)$$

As for the deviatoric part, σ^V is the total mean stress, corresponding to the sum of the stress $\sigma_b{}^V$ of each branch. K_0 and G_0 are the moduli of the elastoplastic branch, while K and G are the sum of the moduli of each branch from *0* to *N*. The damage variable d is related to the maximum positive principal strain $\langle\varepsilon_I\rangle_+$ such that:

$$d = \left(d_1 \sup_t(\langle\varepsilon_I\rangle_+) + d_2\right) \frac{d_3 \sup_t(\langle\varepsilon_I\rangle_+)}{1 - d_3 \sup_t(\langle\varepsilon_I\rangle_+)} \quad (20)$$

where d_1, d_2 and d_3 are material parameters without units. In the previous models, damage – described by the variable c – was related to the stress. Here, damage is due to the largest positive strain in the load history, denoted $\sup_{(t)}(\langle\varepsilon_I\rangle_+)$.

A temperature extension of the model is presented in Le's thesis manuscript (Le, 2007) and a multiaxial failure criterion (the reader should note that failure here means "maximum stress") is detailed in (Caliez et al., 2014; Picart and Pompon, 2016). This criterion takes into account two mechanisms: one on the maximum positive principal strain and another on the maximum positive principal effective stress, both defined in relation to the stress of the elastoplastic branch (index *0*). The first of the two criteria reached indicates the actual failure.

First, a DMA campaign was conducted to determine the longitudinal viscoelastic moduli for a Maxwell model with ten dashpots. The 3D extension is performed using a Poisson's ratio, experimentally measured. In the absence of experimental data highlighting the hardening mechanism, the authors assume an isotropic hardening. This assumption implies that the unloadings are purely elastic and so the secant modulus calculated between the end of the relaxation and the end of the recovery of cyclic tests is supposed to be elastic. The damage is calculated for each cycle as the elastic longitudinal modulus degradation with respect to the first cycle value: $d=(E_0\text{-}E)/E_0$. Plotting the damage evolution as a function of the maximum positive strain (i.e.: transversal strain in compression, longitudinal strain in tension) enables estimation of the coefficients d_1, d_2 and d_3. From cyclic tests again, the inelastic strains at the end of the recoveries are considered as plastic strains. Plotting these plastic strains against the corresponding relaxed stress provides an estimate of the plastic parameters β^*, k and the function R(k). Lastly, the calibration of the failure criterion from multiaxial loadings on M1 is detailed by Picart and Pompon (Picart and Pompon, 2016).

The validation of the model is presented in (Caliez et al., 2014; Le, 2007). The model is confronted with a Brazilian test and three-point bending performed on M1. For the three-point bending test, the experimental force-displacement curve is very well reproduced by the model. For the Brazilian test, the force-displacement curve differs from the experimental curve. For the same displacement, the simulated force is slightly lower than the experimental force and the failure point is slightly underestimated. In addition, the horizontal and vertical strain fields measured by digital image correlation are compared to the finite element simulation. These comparisons show quite a good match. However, since the plasticity is put in parallel with the viscoelasticity, the envelope curves of the cyclic tests are not well reproduced.

For models calibrated on massive specimens, the underestimation observed in the three-point bending test could also be explained by the well-known "size effect" observed on concretes and other brittle materials (Bazant and Planas, 1997). Since this phenomenon is not being investigated for M1, we cannot conclude on its influence.

5.5. Viscoelastic viscoplastic model (VE-VP)

Buechler has proposed a viscoelastic-viscoplastic model (Buechler, 2012b) to which he has later added isotropic damage (Buechler, 2013) in order to reproduce the PBX-9501 behavior. The viscoelasticity is described by a generalized Maxwell model, involving a purely elastic branch and N viscous ones. The viscoplasticity is put in series with the viscoelasticity. It is described by a Drucker-Prager model whose yield strength depends on the cumulative plastic strain and its rate. The non-associated plastic flow combines isotropic and kinematic hardenings. The model is defined in small strains, and the additivity of the strain rates is written as follows:

$$\underline{\underline{\dot{\varepsilon}_{tot}}} = \underline{\underline{\dot{\varepsilon}_{ve}}} + \underline{\underline{\dot{\varepsilon}_{pl}}} + \underline{\underline{\dot{\varepsilon}_{d}}} \tag{211}$$

where $\underline{\underline{\dot{\varepsilon}_{ve}}}$ is the viscoelastic strain rate, $\underline{\underline{\dot{\varepsilon}_{pl}}}$ the viscoplastic strain rate and $\underline{\underline{\dot{\varepsilon}_{d}}}$ the strain rate due to damage. The plasticity criterion takes the following form:

$$f = \sqrt{\frac{2}{3}\left(\underline{\underline{\sigma}}^{D}-\underline{\underline{X}}^{D}\right):\left(\underline{\underline{\sigma}}^{D}-\underline{\underline{X}}^{D}\right)} - A\,(\sigma^{V}-X^{V}) - \sigma_{Y}\left(\overline{\varepsilon_{pl}}, \dot{\overline{\varepsilon_{pl}}}\right) \tag{22}$$

where $\underline{\underline{X}} = \underline{\underline{X}}^{D} + X^{V}\underline{\underline{1}}$ is the kinematic hardening tensor, σ_Y the yield stress and $\overline{\varepsilon_{pl}}$ the cumulative plastic strain. A is an internal friction coefficient of the material defining the Drucker-Prager slope. The non-associated plastic flow is related to the following potential (B being a constant):

$$g = \sqrt{\frac{2}{3}\left(\underline{\underline{\sigma}}^{D}-\underline{\underline{X}}^{D}\right):\left(\underline{\underline{\sigma}}^{D}-\underline{\underline{X}}^{D}\right)} - B\,(\sigma^{V}-X^{V}) - \sigma_{Y}\left(\overline{\varepsilon_{pl}}, \dot{\overline{\varepsilon_{pl}}}\right) \tag{23}$$

The model takes the following general form:

$$\begin{cases} \dot{\sigma}^{V} = \left(K + \dfrac{\widehat{K}}{\phi_1 d}\right)\dot{\varepsilon}_{tot}{}^{V} - \displaystyle\sum_{b=1}^{N}\frac{\sigma_b{}^{V}}{\tau_b} + \frac{K\dot{\lambda}}{\sqrt{\frac{3}{2}+\frac{B^2}{3}}}\frac{B}{3} - \frac{\dot{d}}{d}\sigma^{V} \\ \underline{\underline{\dot{\sigma}}}^{D} = \left(2G + \dfrac{2\widehat{G}}{\phi_2 d}\right)\underline{\underline{\dot{\varepsilon}_{tot}}}^{D} - \displaystyle\sum_{b=1}^{N}\frac{\underline{\underline{\sigma_b}}^{D}}{\tau_b} - \frac{2G\dot{\lambda}}{\sqrt{\frac{3}{2}+\frac{B^2}{3}}}\frac{\sqrt{\frac{3}{2}}\left(\underline{\underline{\sigma}}^{D}-\underline{\underline{X}}^{D}\right)}{\sqrt{\left(\underline{\underline{\sigma}}^{D}-\underline{\underline{X}}^{D}\right):\left(\underline{\underline{\sigma}}^{D}-\underline{\underline{X}}^{D}\right)}} - \frac{\dot{d}}{d}\underline{\underline{\sigma}}^{D} \end{cases} \tag{24}$$

The damage-induced strain $\underline{\underline{\varepsilon_d}}$ is written in volumetric and deviatoric parts:

$$\begin{cases} \widehat{K}\,\varepsilon_d{}^{V} = \phi_1 d\,\sigma^{V} \\ 2\widehat{G}\,\underline{\underline{\varepsilon_d}}^{D} = \phi_2 d\,\underline{\underline{\dot{\sigma}}}^{D} \end{cases} \tag{25}$$

The damage d depends exclusively on the cumulative plastic strain $\overline{\varepsilon_{pl}}$. ϕ_1 and ϕ_2 are parameters without units controlling the damage effectivity (i.e.: whether or not the influence of the damage depends on the loading direction) on the volumetric and deviatoric components. $\widehat{K}$ and $\widehat{G}$ are bulk and shear moduli connecting the stress to the damage and the strain. No more details are given by the author.

The model is parameterized from PBX-9501 experimental results in uniaxial compression (Buechler et al., 2013) but the author points out that the calibration of the slope A is of poor quality due to scattered post-processed experimental data. Moreover, without experimental measurements of transversal strains, the parameter B which controls the plastic volumetric flow cannot be calibrated. The inaccurate fit of the plastic part of the model implies that the damage evolution (related to the cumulative plastic strain) is poorly determined. A comparison of a monotonic compression simulation at $7.5\text{x}10^{-5}$ s^{-1} with two monotonic tests performed at 10^{-5} s^{-1} and 10^{-4} s^{-1} is given in (Buechler 2012b, 2013). According to the author, the result is encouraging because the simulated curve is bordered by the experimental curves, but the model is not validated.

5.6. Elastic viscoplastic model (E-VP)

In the approach proposed by Zubelevicz and coworkers (Zubelewicz et al., 2013) the total strain tensor has three components:

$$\dot{\underline{\underline{\varepsilon}}}_{tot} = \dot{\underline{\underline{\varepsilon}}}_{el} + \dot{\underline{\underline{\varepsilon}}}_{pl}^{ch} + \dot{\underline{\underline{\varepsilon}}}_{pl}^{b} \quad (26)$$

The plasticity is split into two parts. The first, $\dot{\underline{\underline{\varepsilon}}}_{pl}^{ch}$, describes the macroscopic effect of the grain chains dilatancy and shearing with a Drucker-Prager viscoplastic criterion. The second, $\dot{\underline{\underline{\varepsilon}}}_{pl}^{b}$, purely deviatoric, describes the equivalent binder shearing. There is no hardening. The plastic flow accounts for temperature dependence. The elastic strains are linked to the stress by a stiffness tensor affected by an anisotropic damage tensor $\underline{\underline{d}}$ affected by the loading direction. This tensor $\underline{\underline{d}}$ is represented in terms of symmetric tensors depending on the stress state, "turning" for non-monotonic loading.

$$\underline{\underline{\sigma}} = \left(\left(K-\frac{2}{3}G\right)\left(\underline{\underline{1}}-\underline{\underline{d}}\right)\otimes\left(\underline{\underline{1}}-\underline{\underline{d}}\right) + 2G\left(\underline{\underline{1}}-\underline{\underline{d}}\right)\overline{\otimes}\left(\underline{\underline{1}}-\underline{\underline{d}}\right)\right) : \underline{\underline{\varepsilon_{el}}} \quad (27)$$

$$\underline{\underline{d}} = d_c\left(\alpha_{0_c}\,\underline{\underline{1}} + \alpha_{1_c}\,\underline{\underline{\sigma}}^{D} + \alpha_{2_c}\,\underline{\underline{\sigma}}^{D}.\underline{\underline{\sigma}}^{D}\right) + d_t\left(\alpha_{0_t}\,\underline{\underline{1}} + \alpha_{1_t}\,\underline{\underline{\sigma}}^{D} + \alpha_{2_t}\,\underline{\underline{\sigma}}^{D}.\underline{\underline{\sigma}}^{D}\right) \quad (28)$$

The operator $\otimes$ defines the tensor product: $(\underline{a}\otimes\underline{b})_{ijkl} = a_{ij}b_{kl}$, while $\overline{\otimes}$ defines: $(\underline{a}\,\overline{\otimes}\,\underline{b})_{ij} = \frac{1}{2}(a_{ik}b_{jl}+a_{il}b_{jk})$. The brittle damage d_t depends on the full history over time of the strain projection on the t part of the tensor $\underline{\underline{d}}$, and the ductile damage d_c depends on the full history over time of an equivalent plastic strain being then pressure-dependent. The parameters α_{0_t}, α_{1_t}, α_{2_t} (resp. indexed c) are functions of the Lode's angle, and can be assimilated to the damage effectivity as a function of the loading direction.

The 23 parameters of the model are calibrated from stress versus longitudinal strain curves of seven monotonic compression tests and seven tension tests performed on PBX-9502 at five temperatures between -52°C and 74°C and at 10^{-3} to 10^{-5} s^{-1}. It should be noted that it is not specified how the Poisson's ratio is determined without transversal strain measurements. The authors only validate their model using one comparison of the simulated versus experimental failure pattern of a compression sample.

5.7. Microplane formulation applied to pressed explosives (VDT-P)

Taking up the cyclic tests on M1, Benelfellah and coworkers (Benelfellah, 2013; Benelfellah et al., 2014, 2017; Picart et al., 2014) were interested in the induced anisotropy of the material highlighted by these tests. The authors determined longitudinal and transversal elastic moduli for each loading cycle. By tracing these moduli evolutions as a function of the maximum positive strain, they highlight a faster degradation of the transversal modulus than for the longitudinal one, due to an induced anisotropy of the material. The authors also observed that during tests alternating tension and compression loadings, the material recovers its initial stiffness shortly after being compressed. This phenomenon, called unilateral effect, has been observed for granular materials such as concrete (Mazars et al., 1990). The microstructural interpretation given is that the microcracks opened in tension close when the loading direction is reversed; once closed and blocked under the effect of compression, these cracks no longer have an effect on the macroscopic behavior of the material.

The model coupled a damage-induced anisotropy (Benelfellah, 2013; Benelfellah et al., 2014, 2017; Picart et al., 2014) with the plasticity model proposed by Le et al. (2010), denoting $\underline{\underline{\underline{\underline{\mathbb{C}}}}}_d$ the damaged stiffness:

$$\underline{\underline{\sigma}} = \underline{\underline{\underline{\underline{\mathbb{C}}}}}_d : \left(\underline{\underline{\varepsilon_{tot}}} - \underline{\underline{\varepsilon_{pl}}}\right) \quad (29)$$

To describe the anisotropy of the damaged stiffness tensor, Benelfellah et al. have chosen a microplane approach (Benelfellah et al., 2014, 2017). In this model, each microplane is defined by its normal $\underline{n}$ and the elastic strains tensor is split in three components (volumetric, deviatoric and tangential) as follows (Carol and Bazant, 1997):

$$\underline{\underline{\varepsilon_{el}}} = \varepsilon_{V\,el}\,\underline{\underline{V}} + \varepsilon_{D\,el}\,\underline{\underline{D}} + \underline{\underline{\varepsilon_{T\,el}}}.\underline{\underline{T}} \quad (30)$$

where $\underline{\underline{V}}$, $\underline{\underline{D}}$ and $\underline{\underline{\underline{T}}}$ are the tensors of projections on the microplane, expressed as a function of the second and the fourth order unit tensors and the normal vector $\underline{n}$ to the microplane:

$$\underline{\underline{V}} = \frac{1}{3}\,\underline{\underline{1}} \qquad \underline{\underline{D}} = \underline{n}\otimes\underline{n} - \frac{1}{3}\,\underline{\underline{1}} \qquad \underline{\underline{\underline{T}}} = \underline{n}\,\underline{\underline{\underline{I}}} - \underline{n}\otimes\underline{n}\otimes\underline{n} \tag{31}$$

Let us note that the volumetric projection $\underline{\underline{V}}$ is not dependent on the microplane. The damaged stiffness tensor is discretized as a sum on the hemisphere of the stiffness contributions depending on the normal $\underline{n}$ to the microplane:

$$\underline{\underline{\underline{\underline{\mathbb{C}_d}}}} = 3\,k_V\,(1-\alpha_V\,d_V)\,\underline{\underline{V}}\otimes\underline{\underline{V}} + \sum_{\text{hemi-sphere}} 6\,\omega(\underline{n})\left(\mu_D\left(1-\alpha_D(\underline{n})\,d_D(\underline{n})\right)\underline{\underline{D}}(\underline{n})\otimes\underline{\underline{D}}(\underline{n}) + \mu_T\left(1-d_T(\underline{n})\right)\underline{\underline{\underline{T}}}(\underline{n})^{T}\underline{\underline{\underline{T}}}(\underline{n})\right) \tag{32}$$

where d_v, d_D and d_T are the damage variables, α_V and $\alpha_D$the effectivity of the damage (without unit) and k_V, μ_D and μ_T elastic constants defined from the bulk modulus K and the shear modulus G. The damage variables for each direction are defined with respect to the elastic volumetric strains as follows:

$$d_{i=V,D,T} = \max\left(d_i^0,\ \max_t(d_i)\,,\ 1 - \exp(-p\,(a_3F_i)^{a_4})\right) \tag{33}$$

$$p = 1 + \left(a_5\,\mathrm{H}(-\varepsilon_{V\,el}) + \widetilde{a_5}\,\mathrm{H}(\varepsilon_{V\,el})\right)\ k_V\ \langle\varepsilon_{V\,el} - \varepsilon_{V\,el}^{0\,H10}\rangle_+ \tag{34}$$

where a_3 (MPa^{-1}), a_4, a_5 (MPa^{-1}) and $\widetilde{a_5}$ (MPa^{-1}) are material parameters. The damage function never decreases thanks to the term $\max_t(d_i)$ denoting the maximal value over time of d_i. d_i^0 is the value of the "damage" of the virgin material, called pre-damage. The variable p carries the pressure-dependence (here a volume change dependence) where $\varepsilon_{V\,el}^{0\,H10}$ corresponds to the volumetric strain resulting from a hydrostatic compression of 10.8 MPa. The variable F_i is the dual of damage d_i. The volumetric damage d_V depends on the volumetric strain $\varepsilon_{V\,el}$ and effectivity α_V; the deviatoric damage d_D depends on the deviatoric strain $\varepsilon_{D\,el}(\underline{n})$ and effectivity α_D; the tangential damage d_T depends on the tangential strain $\underline{\varepsilon_{T\,el}}(\underline{n})$. The damage is therefore controlled by strain and pressure. The effectivity functions are defined from the Heaviside function H(.) so that the partial derivative of the free energy is continuous even at zero, in respect to a good thermodynamic framework:

$$\begin{cases} \alpha_V = \mathrm{H}(\varepsilon_{V\,el}) \\ \alpha_D(\underline{n}) = \mathrm{H}\left(\varepsilon_{D\,el}(\underline{n})\right) + a_6\mathrm{H}\left(-\varepsilon_{D\,el}(\underline{n})\right) \end{cases} \tag{35}$$

where a_6 is a material parameter without unit.

The total stress tensor from equation (29) can be split as previously into a volumetric and a deviatoric part:

$$\begin{cases} \dot{\sigma}^V = 3\,k_V\left((1-\alpha_V\,d_V)\dot{\varepsilon}_{V\,el} - \alpha_V\,\dot{d}_V\,\varepsilon_{V\,el}\right)\underline{\underline{V}} \\ \underline{\underline{\dot{\sigma}}}^D = \sum_{\text{hemi-sphere}} 6\,\omega(\underline{n})\left(\mu_D\left(1-\alpha_D(\underline{n})\,d_D(\underline{n})\dot{\varepsilon}_{D\,el}(\underline{n}) - \alpha_D(\underline{n})\,\dot{d}_D(\underline{n})\,\varepsilon_{D\,el}(\underline{n})\right)\underline{\underline{D}}(\underline{n})\right. \\ \qquad\qquad \left. + \mu_T\left(1-d_T(\underline{n})\,\underline{\dot{\varepsilon}_{T\,el}}(\underline{n}) - \dot{d}_T(\underline{n})\,\underline{\varepsilon_{T\,el}}(\underline{n})\right)\underline{\underline{\underline{T}}}(\underline{n})\right) \end{cases} \tag{36}$$

The elastic moduli of the material are estimated from triaxial test under a pressure (10 MPa) which induces a collapse of the initial porosity. The k_V modulus is expressed from the bulk modulus under this pressure. The same should be true for μ_D and μ_T, but because the deviatoric effectivity α_D depends only on the deviatoric strain ε_D, the deviatoric shear modulus μ_D cannot be pressure dependent. Finally, the moduli μ_D and μ_T are worth twice the shear moduli measured from uniaxial compression test. The volumetric pre-damage is estimated from the comparison of uniaxial compressions tests (denoted *H0*) and triaxial compression tests with a 10.8 MPa confinement (*H10*): $d_V^0=(K^{H10}-K^{H0})/K^{H10}$. Due to lack of data, pre-damages d_D^0 *and* d_T^0 are neglected. The coefficients a_3 and a_4 are fitted on the triaxial test at 10.8 MPa; a_5 is fitted on the uniaxial compression test and $\widetilde{a_5}$ on the uniaxial tension test; lastly, a_6 is calibrated from three cyclic tests.

The microplane model of Benelfellah does not yet describe viscoelasticity, so the viscosity (relaxation and recovery steps from cyclic tests) is removed from experimental data to be compared

with the simulation. The evolution of the strains is well reproduced, so the induced anisotropy seems to be well described. Further work is necessary on this model for a complete validation.

Recently, Chatti and coworkers (Chatti et al., 2018) have incorporated a viscoelastic component into this model. They add a generalized Maxwell model on the *V*, *D*, *T* directions of each microplane. This work is still ongoing.

5.8. Discussion

A lot of tests were conducted to characterize the thermomechanical behavior of these materials. A wide range of strain rate, temperature and confinement was investigated. Many efforts focused on the (1) viscoelastic response and the determination of time-to-temperature equivalencies. Experiments showed (2) the asymmetric responses (compression versus tension); (3) induced anisotropy due to damage (and then unilateral effect) and/or plasticity (kinematic hardening for M2); (4) pressure-dependent Young's modulus probably due to pre-damage; (5) pressure-, strain rate- and temperature-dependence of elastic modulus and peak stresses; (6) close strain at peak stresses whatever the temperature and the strain rate for a fixed confinement (Figures 5 and 6). Recently, digital image correlation technics have enabled measurement of the heterogeneous macroscopic field of strain at the surface of the sample. These data can be used to validate models. Let us now compare data to constitutive laws to yield some routes for future development.

The phenomena taken into account by the previous models are listed in Table 3. It must be noted that all the models, excluding VE-P and VDT-P, are calibrated for stress versus longitudinal strain curves only, for the compression and tension tests. Measuring only the longitudinal strain prevents observation of the volumetric and the deviatoric responses and a possible induced anisotropy. Historically, the experimentally observed non-linear behavior was attributed mainly to sophisticated damage rules neglecting plasticity. The "brittle material" point of view has progressively been completed by viscoelasticity to deal with temperature and strain rate dependencies. Recently, several studies have integrated a plastic mechanism as experiments reveal irreversible strains.

Table 3*. Summary of the content of the models and materials on which the parameters have been fitted.*

				SCRAM	VS	VS-VP	VE-P	VE-VP	E-VP	VDT-P
Material	PBX-9501 (HMX-based)			√	√					
	PBX-9502 (TATB-based)					√			√	
	CEA-M1 (HMX-based)						√			√
	CEA-M2 (TATB-based)					√				
Model contents	Elasticity	Hooke's law	Volumetric	√	√	√			√	√
			Deviatoric	√					√	√
		Viscoelasticity	Volumetric				√	√		
			Deviatoric		√	√	√	√		
	Irreversibility / plasticity	Viscoplasticity				√	√	√	√	√
		Volumetric					√	√	√	√
		Deviatoric		√		√	√	√	√	√
		Isotropic hardening				√	√	√		√
		Kinematic hardening		√				√		
		Non-associated flow				√	√	√		√
		Pressure-dependence					√	√	√	√
	Damage	Isotropic			√	√	√	√		
		Anisotropic		√					√	√

Pressure-dependence		√		√	√		√	√
Temperature-dependence					√		√	
Independent failure criterion					√			√

The guidelines for a future macroscopic "unified constitutive law" for HMX- and TATB-based pressed PBXs are now discussed. The concordance of the monotonic tests and the envelope curves of cyclic tests, regardless of the temperature, the strain rate or the type of binder (M1, M2, PBX-9501), encourages the use in a reference model of so-called "serial" laws, where an irreversible mechanism (plasticity, damage, etc.) ensures the non-linearity of the response. This is the assumption made in SCRAM and its evolutions (VS, VS-VP). In the first M1 constitutive law (VE-P), the plasticity is in parallel with the viscoelasticity, which prevents the envelope curve from being well reproduced. The second model (VDT-P) combines elasticity with damage and plasticity in series.

Most of the models take into account a linear viscoelastic behavior which is experimentally validated for M1, M2 and PBX-9501 and -9502, as long as the strains remain low. This first viscous mechanism enables strain rate and temperature dependencies to be accounted for. The literature review shows that time-temperature equivalence is generally experimentally validated for PBXs. Williamson et al. (2008) have successfully compared time-temperature equivalence to ultimate stresses in compression for EDC-37. Thompson et al. (2012) do the same for PBX-9501, comparing the ultimate strain and the secant modulus at 25% of the peak-stress too. However, there is no real demonstration where a viscoelastic model would be compared to long duration and high temperature creep or relaxation. Furthermore, the "damage" observed on M1 and M2 at low temperature, even if it is thermally activated, prevents the application of time-temperature equivalence below 0°C. Moreover, crossing the glass transition temperature could alter the accuracy of usual equivalence. Thus, time-temperature must be part of a future model, but attention will be paid to accurately defining its field of use. As shown in Table 3, linear viscoelasticity is embedded in VS, VS-VP, VE-P and VE-VP.

Some models consider damage as inducing additional strain (SCRAM, VS, VS-VP, VE-VP) while for others (VE-P, E-VP, and VDT-P), damage affects the (visco)elastic stiffness. However, by comparing the final equations of these models (equations 10, 13, 19, 24), it is clear that these two modelling choices are the same. The damage is purely deviatoric in VS and VS-VP while it is also volumetric in VE-P and VE-VP. The bulk modulus K is affected by the damage (1-d) in VE-P and by $1+\widehat{K}/K\phi_1 d(\overline{\varepsilon_{pl}})$ in VE-VP. The shear modulus G is affected by the damage $\left(1+c^3/a^3\right)^{-1}$ in VS and VS-VP; by (1-d) in VE-P; and by $1+\widehat{G}/G\phi_2 d(\overline{\varepsilon_{pl}})$ in VE-VP. In VS and its derivative VS-VP, for a constant damage ($\dot{c}=0$), the crack length c affects the shear modulus G but also the viscous characteristic times. To our knowledge, this effect has not been experimentally demonstrated. In the VE-P, VE-VP and VDT-P models, the damage d only affects the instantaneous elastic moduli. Since M1 shows a pressure-dependence for the initial elastic properties, the authors recommend implementing damage also for the isotropic part of the constitutive law. This will enable pre-damage evolution to be tracked, as it is in the VDT-P model.

The extensive experimental study of M1 and M2 have showed that damage develops (late for M2) and that its nature is strongly anisotropic for M1. It therefore seems inevitable to incorporate induced anisotropy into future models to reproduce complex stress states and especially the effectivity of the damage seen on M1. Only SCRAM, E-VP and VDT-P described induced anisotropic damage.

The question of the damage evolution law is still open. Two regimes are distinguished (one in extension, the other in compression) in SCRAM, VS-VP and VDT-P by the Heaviside functions of the normal stress, the mean stress and the elastic volumetric strain, respectively. The variable driving damage in the models with/without anisotropic damage is either the cumulative plastic strain (VE-VP), the equivalent stress (VS) or the largest positive strain (VE-P, VDT-P). The experimental study of M1 is favorable to damage controlled by positive strain and pressure. As regards the behavior of M2, it is not possible to draw conclusions without experimental measurement of damage close to the peak stress. It should be pointed out that since the strain of pressed explosives remains low (quasi-brittle materials), the difficult problem of the rotation of anisotropy axes does not have to be treated. The effectivity of the damage, observed on M1, is treated in SCRAM, VS-VP and VDT-P. In VDT-P, the effectivity functions are related to the strain to satisfy thermomechanical considerations, but no

experimental evidence justifies this. SCRAM and VS-VP generate a unilateral effect by using Heaviside functions of normal and mean stress respectively. Unfortunately, dealing with anisotropic damage prevents the characterization of the contribution of each microcracks system (each system is orientated along a plane), the recorded macroscopic damage being the consequence of all of them. As long as the unified model is to be used below maximum stress, and for moderate localization of strain, research will have to follow micromechanical model conclusions.

Cyclic tests on M1, M2 and PBX-9501 revealed irreversible strains after unloading. For some materials, the plasticity threshold appears to depend on pressure (M1, EDC-37), temperature (M1, M2 only beyond the glass transition) and strain rate (M1). The initial yield stress of M1 is pressure- and strain rate-dependent, which is not the case for M2.

Comparison between constitutive equations 10, 13, 19, 24 highlights that the damage affects plasticity in VS-VP and VE-P models while plasticity drives damage in VE-VP. There is no experimental data to allow any conclusions to be made. Our opinion is that for moderate loadings (low confinement and quasistatic strain rates), macroscopic loss of stiffness and irreversible strains are the consequence of microcracks nucleation, opening/closing, growth, and relative displacement and friction of the lips of cracks. However, Vial (2013) also demonstrated that plasticity occurs in the HMX crystals of the M1 composition when they are sheared under low confinement. Microstructural post-mortem characterizations are missing, which would enable separation of the contribution of microcracks and crystal plasticity to the irreversible strains. Several routes could be followed only involving damage (see, for example, the work of Bargellini et al. (2008) for concretes), plasticity, or both, as in all the models previously presented. In the latter, the loss of stiffness is related to damage and the irreversible strain to a “plasticity” mechanism. This is the case in VDT-P, friction of microcracks being incorporated through a plastic law and an effective stress tensor.

A dilating plastic behavior has been demonstrated for M1 and is strongly suspected for M2. Yet only the VE-P, VE-VP, E-VP and VDT-P models describe a volumetric plasticity. In addition, the tests on M1 highlighted the need for a non-associated flow law, implemented in all models except SCRAM and VS.

We have also shown that a combined isotropic and kinematic hardening, not present in any model, is necessary to model at least the behavior of M2.

For the modelling of M1 (VE-P and VDT-P), failure (i.e.: maximum stress) and damage are totally dissociated. It has been experimentally demonstrated that damage depends on the loading history while failure depends only on the instantaneous stress and strain. One of the two failure criteria adopted for M1 is a function of the largest positive strain while the second takes account of the positive effective stress to describe the failure in tension states. These two failure modes have been favorably compared to multiaxial data in Picart and Pompon (2016). No failure criteria are presented in the other models.

The preceding remarks do not enable a model to be selected for this class of energetic materials, particularly when they are subjected to complex loads. Our guidelines for the development of a unified model are therefore as follows:

- The use of an additive decomposition of the strain into mechanisms rather than incorporating, for example, the plasticity as a new branch in a parallel Maxwell model (additivity of the viscous stresses).
- Because it is probably the hardest task, a mechanism for loading-induced anisotropic damage must first be taken into account. The two models SCRAM and VDT-P can serve as a basis for future development. Damage evolution could be linked to penny-shaped microcrack nucleation, growth and friction using a mean field homogenization approach. Many rules have been reported above, the difficulty being their experimental verification at the microscale. The second route, as in VDT-P, is to use a macroscopic phenomenological description of the damage (and of its effectivity). We have observed a close relation between damage evolution and the total strain tensor (positive strain for example). An isotropic pre-damage and its evolution with at least the pressure is also required.
- A linear viscoelasticity part for pressed PBXs (using a Maxwell’s-like approach for example), including a time-temperature equivalence which domain of validity must be accurately defined.

- Irreversible strains description requires a (visco)plastic mechanism. Using an effective stress will help to separate the damage effect from the plasticity effect. The plastic threshold could be, for example, of the Drucker-Prager's type (pressure-dependent) but a non-associated flow rule must absolutely be proposed.
- Isotropic hardening is usually stated, but data show that a kinematic hardening rule is required to model the plastic anisotropy which could develop during complex loadings. This mechanism is an evidence for M2, while an in-depth analysis of M1 data is required.
- Multiaxial failure criteria could be separately proposed and implemented in the model to predict the ultimate loadings. These criteria must be calibrated on multiaxial tests at least, such as the one stated in section 3.10. For a pyrotechnic structure, such failures relate to the peak stresses rather than the failure stress.

Since improving models is closely related to experiments, the investigation of the possible non-linear viscoelasticity of such material is required. DMA measurements are made at low pressure. The question is to observe how the viscoelasticity evolves when the confinement, and thus the strain, increases.

Monotonic curves being the consequence of many deformation mechanisms, these data give some guidelines but are unusable for improving models. Moreover, only a few non-uniaxial experiments were done. Loadings at constant deviatoric to mean stress ratios, torsion experiments, tension under confinement, or perfect triaxial experiments (principal stresses separately loaded) would help to a better understanding of these quasi-brittle materials. Also, different loading conditions must be mixed. Tension under confinement, uniaxial compression at different temperatures and strain rates or conventional triaxial experiments at different pressures and strain rates (see Vial 2013 for a first investigation) or temperatures could help to understand how the deformation mechanisms interact.

Finally, the study of M1 and M2 showed several surprising effects: (1) thermal damage at low temperature, different from the ratchet growth phenomenon (based on the glass transition temperature) observed on PBX-9501 and PBX-9502; (2) a non-monotonic effect of pressure on the volumetric behavior and on the elastic moduli, notably between 5 and 10 MPa; (3) a possible size effect, already observed on concrete.

6. Conclusion

Ensuring the safety and reliability of pyrotechnic structures is obviously indispensable. Nowadays this is done by numerical simulations, and the various materials which make up the pyrotechnic structure must be accurately modelled. An exhaustive state of the art of quasistatic mechanical tests provided in the literature has been proposed for pressed HMX- and TATB-based PBXs. This analysis has shown that few experimental campaigns have been carried out on these materials (except for an HMX-based material, the explosive composition M1), resulting in many assumptions about their behavior. An exhaustive characterization of CEA M2 has been provided in this paper to fill the gap on TATB-based PBXs. This material shows strain rate-, temperature- and pressure-dependence, inelastic strain and a load-induced anisotropy.

Since HMX- and TATB-based PBXs have similar macroscopic properties, a universal constitutive law is attainable for this class of materials. Although the mechanisms (elasticity, viscosity, damage, plasticity, etc.) implemented in this future law could be the same, each explosive composition would have its own set of parameters. Thus, a critical review of already proposed constitutive laws has been made. It has been shown that most of the models are poorly based on experimental facts, explaining the variety of assumptions made by their authors. Conversely, the constitutive laws proposed for M1 enables the simulation of complex loading conditions. The additivity of deformation mechanisms is justified for PBXs, as is the use of a linear viscoelastic component. A rigorous confirmation of their time-to-temperature equivalence is still needed, as is an in-depth study of the viscoelasticity linearity at high stress levels. An anisotropic damage law is advised by the authors, mainly controlled by the positive strain and the pressure, with effectivity. But how effectivity is controlled remains an open question. SCRAM or VDT-P could serve as a basis for future developments. This paper shows that kinematic hardening must be introduced in the constitutive law, and the model proposed for M1 will therefore reconsider this observation. Lastly, the described experimental database has shown unusual

phenomena at low temperature or intermediate pressures, and this requires future work to understand the causes.

The development of such a model will need a lot of internal variables, such as - at least - the elastic viscous stresses, dozens of damage variables depending on the spatial discretization of the unit sphere, and five variables per kinematic hardening mechanism. Such is the cost of yielding accurate finite element predictions of the thermomechanical response of these explosive compositions when subjected to complex loading paths.

7. Acknowledgements

This work has been carried out within the framework of the research program of the Corresponding Research Laboratory (CosMa), a joint laboratory combining CEA Le Ripault and the Gabriel Lamé Mechanical laboratory.

The authors would like to thank J.L. Brigolle, T. Peyre and C. Pompon for their involvement in the experimental part of this paper, and the reviewers for their comments and suggestions.

8. References

[1] **Addessio F.L., Johnson J.L. (1990)** – A constitutive model for the dynamic response of brittle materials. *Journal of Applied Physics 67(7), 3275-3286. https://doi.org/10.1063/1.346090*

[2] **Ambos A., Willot F., Jeulin D., Trumel H. (2015)** – Numerical modeling of the thermal expansion of an energetic material. *International Journal of Solids and Structures 60-61, p. 125-139. https://doi.org/10.1051/mattech/2015019*

[3] **Arora H., Tarleton E., Li-Mayer J., Charalambides M.N., Lewis D. (2015)** – Modelling the damage and strain process in a plastic bonded explosive microstructure under tension using the finite element method. *Computational Materials Science 110, p. 91-101. https://doi.org/10.1016/j.commatsci.2015.08.004*

[4] **Bargellini R., Halm D., Dragon A. (2008)** – Modelling quasi-brittle behaviour: discrete approach coupling anisotropic damage growth and frictional sliding. *European Journal Mechanics – A/Solids 27(4), p. 564-581.*

[5] **Bazant Z.P., Planas J. (1997)** – Fracture and size effect in concrete and other quasi-brittle materials. *CRC Press, New-York (USA).*

[6] **Belmas R., Reynaud J., Sorel J. (1982)** – Simulation numérique du comportement viscoélastique non-linéaire d'un matériau explosif. *Propellants, Explosives, Pyrotechnics 7, p. 8-11. https://doi.org/10.1002/prep.19820070104*

[7] **Benelfellah A. (2013)** – Contribution à la modélisation de l'anisotropie induite par endommagement d'un matériau agrégataire énergétique. *PhD thesis, Université François Rabelais de Tours.*

[8] **Benelfellah A., Frachon A., Gratton M., Caliez M., Picart D. (2014)** – Analytical and numerical comparison of discrete damage models with induced anisotropy. *Engineering Fracture Mechanics 121/122, p. 28-39. https://doi.org/10.1016/j.engfracmech.2014.03.022*

[9] **Benelfellah A., Frachon A., Gratton M., Caliez M., Picart D. (2017)** – VDT microplane model with anisotropic effectiveness and plasticity. *Mechanics & Industry 18(607). https://doi.org/10.1051/meca/2017032*

[10] **Bennett J.G., Haberman K.S., Johnson J.N., Asay B.W., Henson B.F. (1998)** – A constitutive model of the non-shock ignition and mechanical response of high-explosives. *Journal of the Mechanics and Physics of Solids 46, p. 2303-2322. https://doi.org/10.1016/S0022-5096(98)00011-8*

[11] **Benouniche S. (1979)** – Modélisation de l'endommagement du béton par microfissuration en compression. *PhD thesis, Université de Paris VI.*

[12] **Blumenthal W.R., Gray G.T. III, Idar D.J., Holmes M.D., Scott P.D., Cady C.M., Cannon D.D. (1999)** – Influence of temperature and strain rate on the mechanical behaviour of PBX 9502 and Kel-F 800™. *AIP Conference Proceedings 505, p. 671-674. https://doi.org/10.1063/1.1303562*

[13] **Bodner S. R. (1987) –** Review of a Unified Elastic—Viscoplastic Theory. *Unified Constitutive Equations for Creep and Plasticity, Springer Dorddrecht. https://doi.org/10.1007/978-94-009-3439-9_6.*

[14] **Browning R.V., Gurtin E.M., Williams W.O. (1984)** – A one-dimensional viscoplastic constitutive theory of filled polymers. *International Journal of Solids and Structures 20(11/12), p. 921-934. https://doi.org/10.1016/0020-7683(84)90081-7*

[15] **Buechler M.A. (2012a)** – Observed physical processes in mechanical tests of PBX 9501 and recommendations for experiments to explore a possible plasticity/damage threshold. *Los Alamos National Laboratory, report n° LA-UR-12-21072.*

[16] **Buechler M.A. (2012b)** – Viscoelastic-viscoplastic combined hardening constitutive model based on the Drucker-Prager yield and flow potentials. *Los Alamos National Laboratory, report n° LA-UR-12-24895.*

[17] **Buechler M.A. (2013)** – Viscoelastic-viscoplastic damage model development, parameters estimation, and comparison to PBX9501 experimental data. *Los Alamos National Laboratory, report n° LA-UR-13-DRAFT.*

[18] **Buechler M.A., DeLuca R., Thompson D.G. (2013)** – Review of cyclic experiments performed on PBX9501. *Los Alamos National Laboratory, report n° LA-UR-13-27212.*

[19] **Buechler M.A., Luscher D.J. (2014)** – A semi-implicit integration scheme for a combined viscoelastic-damage model of plastic bonded explosives. *International Journal for Numerical Methods in Engineering 99, p. 54-78. https://doi.org/10.1002/nme.4672*

[20] **Caliez M., Gratton M., Frachon A., Benelfellah A., Picart D. (2014)** – Viscoelastic plastic model and experimental validation for a granular energetic material. *International Journal of Energetic Materials and Chemical Propulsion 13, p. 525-537. https://doi.org/10.1016/j.engfracmech.2014.09.009*

[21] **Cambou B., Lanier J. (1988)** – Induced anisotropy in cohesionless soil: experiments and modelling. *Computers and Geotechnics 6, p. 291-311. https://doi.org/10.1016/0266-352X(88)90071-7*

[22] **Carol I., Bazant Z.P. (1997)** – Damaged and plasticity in microplane theory. *International Journal of Solids and Structures 34(29). https://doi.org/10.1016/S0020-7683(96)00238-7.*

[23] **Chatti M. (2018)** – Etude expérimentale et modélisation du comportement mécanique d'un matériau agrégataire. *PhD thesis https://tel.archives-ouvertes.fr/tel-02415344*

[24] **Chatti M., Frachon A., Gratton M., Caliez M., Picart D., Aït Hocine N. (2018)** – Modelling of the viscoelastic behaviour with damage induced anisotropy of plastic-bonded explosive based on the microplane approach. *International Journal of Solids and Structures 168, p. 13-25. https://doi.org/10.1016/j.ijsolstr.2018.08.018*

[25] **Chen P.W., Huang F.L., Ding Y.S. (2007)** – Microstructure, strain and failure of polymer bonded explosives. *Journal of Materials Science 42, p. 5272-5280. https://doi.org/10.1007/s10853-006-0387-y*

[26] **Clements B.E., Mas E.M. (2004)** – A theory for plastic-bonded materials with a bimodal size distribution of filler particles. *Modelling and Simulation in Materials Science and Engineering 12, p. 407-421. https://doi.org/10.1088/0965-0393/12/3/004*

[27] **Cunningham B.J., Gagliardi F.J., Ferranti L. (2013)** – Low strain rate measurements on explosives using DIC. *Application of Imaging Techniques to Mechanics of Materials and Structures, Volume 4. Springer, New York, NY, p. 25-31. https://doi.org/10.1007/978-1-4419-9796-8_5*

[28] **Dienes J.K. (1978)** – A statistical theory of fragmentation. 19th US Rock Mechanics Symposium, American Rock Mechanics Association.

[29] **Dienes J.K. (1996)** – A unified theory of flow, hot-spots, and fragmentation with an application to explosive sensitivity. *High Pressure Shock Compression of Solids II. Springer, New York, NY, p. 366-398. https://doi.org/10.1007/978-1-4612-2320-7_14*

[30] **Dienes J.K., Zuo Q.H., Kershner J.D. (2006)** – Impact initiation of explosives and propellants via statistical cracks mechanics. *Journal of the Mechanics and Physics of Solids 54, p. 1237-1275. https://doi.org/10.1016/j.jmps.2005.12.001*

[31] **Ellis K., Leppard C., Radesk H. (2005)** – Mechanical properties and damage evaluation of UK PBX. *Journal of Materials Science 40(23), p. 6241-6248. https://doi.org/10.1007/s10853-005-3148-4*

[32] **Funk D.J. Laabs G.W., Peterson P.D., Asay B.W. (1996)** – Measurements of the stress/strain response of energetic materials as a function of strain rate and temperature: PBX 9501 and Mock 9501. *AIP Conference Proceedings 370, p. 145-148. https://doi.org/10.1063/1.50735*

[33] **Gagliardi F.J., Cunningham B.J. (2007)** – Creep testing plastic-bonded explosives in uni-axial compression. *Society for Experimental Mechanics 11th International Congress, Orlando (USA), June 02-05, 2007.*

[34] **Gagliardi F.J., Cunningham B.J. (2009)** – Axial torsion testing of plastic bonded explosives to failure. *Society for Experimental Mechanics Annual Conference, Albuquerque (USA), June 01-04, 2009.*

[35] **Gasnier J.B., Willot F., Trumel H., Jeulin D., Biessy M. (2018)** – Thermoelastic properties of microcracked polycrystals. Part II: The case of jointed polycrystalline TATB. *International Journal of Solids and Structure 155, p. 257-274. https://doi.org/10.1016/j.ijsolstr.2018.07.025*

[36] **Gotuwka V. (1999) –** Etude expérimentale du comportement mécanique des Bétons à Très Hautes Performances sous sollicitations multiaxiales simples et complexes. *PhD thesis, Université de Lille I.*

[37] **Gratton M., Gontier C., Rja Fi Allah S., Bouchou A., Picart D. (2009)** – Mechanical characterisation of a viscoplastic material sensitive to hydrostatic pressure. *European Journal of Mechanics A/Solids 28(5), p. 935-947. https://doi.org/10.1016/j.euromechsol.2009.03.002*

[38] **Gray G.T. III, Idar D.J., Blumenthal W.R., Cady C.M., Peterson P.D. (1998)** – High- and low-strain rate compression properties of several energetic material composites as a function of strain rate and temperature. *11th Detonation Symposium, Snowmass (USA), August 31 – September 4, 1998.*

[39] **Hackett R.M., Bennett J.G. (2000)** – An implicit finite element material model for energetic particulate composite materials. *International Journal for Numerical Methods in Engineering 49(9), p. p. 1191-1209. https://doi.org/10.1002/1097-0207(20001130)49:9<1191::AID-NME997>3.0.CO;2-V*

[40] **Idar D.J., Larson S.A., Skidmore C.B., Wendelnerger J.R. (2000)** – PBX 9502 tension analysis. 23rd Aging, Compatibility, and Stockpile Stewardship Conference, Livermore (USA), November 14-16, 2000.

[41] **Lanier J., Di Prisco C., Nova R. (1991) –** Etude expérimentale et analyse théorique de l'anisotropie induite du sable d'Hostun. *Revue Française de Géotechnique 57, p. 59-74. https://doi.org/10.1051/geotech/1991057059*

[42] **Le V.D. (2007)** – Modélisation et identification du comportement plastique visco-élastique endommageable d'un matériau. *PhD thesis, Université François Rabelais de Tours.*

[43] **Le V.D., Gratton M., Caliez M., Frachon A., Picart D. (2010)** – Experimental mechanical characterization of plastic-bonded explosives. *Journal of Materials Science 45(21), p. 5802-5813. https://doi.org/10.1007/s10853-010-4655-5*

[44] **Liu C., Thompson D.G. (2010)** – Macroscopic crack formation and extension in pristine and artificially aged PBX 9501. *14th International Detonation Symposium, Coeur d'Alene (USA), April 11-16, 2010.*

[45] **Liu C., Thompson D.G. (2014)** – Crack initiation and growth in PBX 9502 high explosive subject to compression. *Journal of Applied Mechanics 81(10), 101004. https://doi.org/10.1115/1.4028087*

[46] **Liu M., Huang X.C., Wu Y.Q., Chen C.J., Huang F.L. (2019)** – Numerical simulations of the damage evolution for plastic-bonded explosives submitted to complex stress states. *Mechanics of Material 139, 103179. https://doi.org/10.1016/j.mechmat.2019.103179*

[47] **Mazars J., Berthaud Y., Ramtani S. (1990) –** The unilateral behaviour of damaged concrete. *Engineering Fracture Mechanics 35 (4-5), p. 629-635. https://doi.org/10.1016/0013-7944(90)90145-7*

[48] **Peeters R.L., Hackett R.M. (1981)** – Constitutive modeling of plastic-bonded explosives. *Experimental Mechanics, 21(3), p. 111-116. https://doi.org/10.1007/BF02326367*

[49] **Picart D. (1993)** – Comportement et mise en forme d'un explosive agrégataire. PhD thesis. https://www.theses.fr/1993DENS0007.

[50] **Picart D., Benelfellah A., Brigolle J.L., Frachon A., Gratton M., Caliez M. (2014)** – Characterization and modeling of the anisotropic damage of a high-explosive composition. *Engineering Fracture Mechanics 131, p. 525-537. https://doi.org/10.1016/j.engfracmech.2014.09.009*

[51] **Picart D., Brigolle J.L. (2010)** – Characterization of the viscoelastic behaviour of a plastic-bonded explosive. *Materials Science and Engineering A 527 (29-30),* p. 7826-7831. *https://doi.org/10.1016/j.msea.2010.08.057*

[52] **Picart D., Pompon C. (2016)** – Experimental characterization of the multiaxial failure of a plastic-bonbed explosive. *International Journal of Energetic Material and Chemical Propulsion 15(2), 141-165. https://doi.org/10.1615/IntJEnergeticMaterialsChemProp.2016013662*

[53] **Rae P.J., Goldrein H.T., Palmer S.J.P., Field J.E., Lewis A.L. (2002)** – Quasi-static studies of the strain and failure of β-HMX based polymer bonded explosives. *Proceedings of the Royal Society of London. Serie A: Mathematical, Physical and Engineering Sciences 458(2019), p.743-762. https://doi.org/10.1098/rspa.2001.0894*

[54] **Rangaswamy P., Thompson D.G., Liu C., Lewis M.W. (2010)** – Modeling the mechanical response of PBX 9501. *14th International Detonation Symposium, Coeur d'Alene (USA), April 11-16, 2010.*

[55] **RjaFiAllah S. (2006)** – Modélisation du comportement mécanique d'un matériau agrégataire. *PhD thesis, Université François Rabelais de Tours.*

[56] **Schwarz R.B., Brown G.W., Thompson D.G., Olinger B.W., Furmanski J., Cady H.H. (2013)** – The effect of shear strain on texture in pressed plastic bonded explosives. *Propellants, Explosives, Pyrotechnics 38, p. 685-694. https://doi.org/10.1002/prep.201200204*

[57] **Shunk D. (2013)** – PBX 9502 literature review: an engineering perspective. *Los Alamos National Laboratory, report n° LA-UR-13-21673.*

[58] **Skidmore C.B., Idar D.J., Son S.F., Sander R.K. (1998)** – Ageing and PBX 9502. Conference on Life Cycles of Energetic Material, Fullerton (USA), March 29 – April 1, 1998.

[60] **Tan H., Huang Y., Liu C., Ravichandran G., Inglis H.M., Geubelle P.H. (2007)** – The uniaxial tension of particulate composite materials with nonlinear interface debonding. *International Journal of Solids and Structures 44(6), p. 1809-1822. https://doi.org/10.1016/j.ijsolstr.2006.09.004*

[61] **Tan H., Liu C., Huang Y., Geubelle P.H. (2005)** – The cohesive law for the particle/matrix interfaces in high explosives. *Journal of the Mechanics and Physics of Solids 53(8), p. 1892-1917. https://doi.org/10.1016/j.jmps.2005.01.009*

[62] **Thompson D.G. (2002)** – Results of PBX 9501 and PBX 9502 round-robin quasi-static tension tests from JOWOG-9/39 focused exchange. *24th Aging, Compatibility, and Stockpile Stewardship Conference and Proceedings, BWXT Pantex, Amarillo (USA), April 30 – May 2, 2002.*

[63] **Thompson D.G., Wright W.J. (2004)** – Mechanical Properties from PBX 9501 pressing study. *AIP Conference Proceedings 706, 503, https://doi.org/10.1063/1.1780287*

[64] **Thompson D.G., Brown G.W., Olinger B., Mang J.T., Patterson B., DeLuca R., Hagelberg S. (2010)** – The effects of TATB ratchet growth on PBX 9502. *Propellants, Explosives, Pyrotechnics 3(6), p. 507-513. https://doi.org/10.1002/prep.200900067*

[65] **Thompson D.G., DeLuca R., Brown G.W. (2012a)** – Time-temperature analysis, tension and compression in PBXs. *Journal of Energetic Materials 30(4), p. 299-323. https://doi.org/10.1080/07370652.2011.569831*

[66] **Thompson D.G., DeLuca R., Brown G.W., Sandstrom M.M., Hagelberg S., Giambra A.M., Hill L.G. (2012b)** – Ratchet growth experiments on TATB and PBX 9502. *AIP Conference Proceedings 1426(1), p. 745-748. https://doi.org/10.1063/1.3686386*

[67] **Vial J. (2013) –** Etude expérimentale et numérique des modes de déformation d'un explosif comprimé. *PhD thesis, Université d'Orléans.*

[68] **Wiegand D.A., Redingus B., Ellis K., Leppard C. (2011)** – Pressure and friction dependent mechanical strength-cracks and plastic flow. *International Journal of Solids and Structures 48(11-12), p. 1617-1629. https://doi.org/10.1016/j.ijsolstr.2011.01.025*

[69] **Williamson D.M., Palmer S.J.P., Proud W.G., Govier R. (2007)** – Brazilian disc testing of a UK PBX above and below the glass transition temperature. *AIP Conference Proceedings 955(1), p. 803-806. https://doi.org/10.1063/1.2833246*

[70] **Williamson D.M., Siviour C.R., Proud W.G., Palmer S.J., Govier R., Ellis K., Blackwell P., Leppard C. (2008)** – Temperature-time response of a polymer bonded explosive in compression (EDC-37). *Journal of Physics D: Applied Physics 41, 085404. https://doi.org/10.1088/0022-3727/41/8/085404.*

[71] **Wu Y.Q., Huang F.L. (2009)** – A micromechanical model for predicting combined damage of particles and interface debonding in PBX explosives. *Mechanics of Materials 41(1), p. 27-47. https://doi.org/10.1016/j.mechmat.2008.07.005*

[72] **Zubelewicz A., Thompson D.G., Ostoja-Starzewski M., Ionita A., Shunk D., Lewis M.W., Lawson J.C. Kale S., Koric S. (2013)** – Fracture model for cemented aggregates. *AIP Advances 3(1), 012119. https://doi.org/10.1063/1.4789791*

Highlights

- A literature review is proposed about (1) the constitutive laws devoted to HMX- and TATB-based PBXs and (2) the few data used to fit the parameters.
- An exhaustive database (with an in-depth description of each experiments) obtained on a TATB-based PBX is detailed.
- Mix with already published data on PBXs, the latter database gives the opportunity to draw the characteristic behavior of pressed plastic-bonded explosives.
- It highlights the mechanisms needed in future unified constitutive laws for this class of materials.

Proposed reviewers

Darla Thompson, Los Alamos, USA, dkgraff@lanl.gov

David Williamson, Cavendish Lab, UK, dmw28@cam.ac.uk

Matthew Lewis, Los Alamos, USA, mlewis@lanl.gov

Bruce Cunningham, Lawrence Livermore, USA, cunningham1@llnl.gov

Min Zhou, Georgia Institute of Technology, min.zhou@gatech.edu

Carole Nadot, Laboratoire P', ENSMA, carole.nadot@ensma.fr

Authors' agreement

- The paper is not concurrently submitted for publication elsewhere
- The paper, in its entirety, in part, or in a modifies version, has not been published elsewhere
- The paper has not previously been submitted for possible publication elsewhere

Declaration of interests

☒ The authors declare that they have no known competing financial interests or personal relationships that could have appeared to influence the work reported in this paper.

☐The authors declare the following financial interests/personal relationships which may be considered as potential competing interests: